

LEARNING LOW-DIMENSIONAL NONLINEAR STRUCTURES FROM HIGH-DIMENSIONAL NOISY DATA: AN INTEGRAL OPERATOR APPROACH

Xiukai Ding ^{*1} and Rong Ma ^{†2}

¹Department of Statistics, University of California, Davis

²Department of Statistics, Stanford University

Abstract

We propose a kernel-spectral embedding algorithm for learning low-dimensional nonlinear structures from high-dimensional and noisy observations, where the datasets are assumed to be sampled from an intrinsically low-dimensional manifold and corrupted by high-dimensional noise. The algorithm employs an adaptive bandwidth selection procedure which does not rely on prior knowledge of the underlying manifold. The obtained low-dimensional embeddings can be further utilized for downstream purposes such as data visualization, clustering and prediction. Our method is theoretically justified and practically interpretable. Specifically, we establish the convergence of the final embeddings to their noiseless counterparts when the dimension and size of the samples are comparably large, and characterize the effect of the signal-to-noise ratio on the rate of convergence and phase transition. We also prove convergence of the embeddings to the eigenfunctions of an integral operator defined by the kernel map of some reproducing kernel Hilbert space capturing the underlying nonlinear structures. Numerical simulations and analysis of three real datasets show the superior empirical performance of the proposed method, compared to many existing methods, on learning various manifolds in diverse applications.

1 Introduction

With rapid technological advancements in data collection and processing, massive large-scale and high-dimensional datasets are widely available nowadays in diverse research fields such as astronomy, business analytics, human genetics and microbiology. A common feature of these datasets is that their statistical and geometric properties can be well understood via a meaningful low-rank representation of reduced dimensionality. Learning low-dimensional structures from these high-dimensional noisy data is one of the central topics in statistics and data science. Moreover, nonlinear structures have been found predominant and intrinsic in these real-world datasets, which may not be easily captured or preserved in commonly used linear or quasi-linear methods such as principal component analysis (PCA), singular value decomposition (SVD) [38] and multidimensional scaling (MDS) [12]. As a longstanding and well-recognized technique for analyzing

*Email: xcading@ucdavis.edu

†Email: rongm@stanford.edu

datasets with possibly intrinsic nonlinear structures, kernel methods have been shown effective in various applications ranging from clustering and data visualization to classification and prediction [56, 34, 43]. On the other hand, spectral methods, as a fundamental tool for dimension reduction, are oftentimes applied in combination with kernel methods to better capture the underlying low-dimensional nonlinear structure in the data. These approaches are commonly referred as nonlinear dimension reduction techniques; see Section 1.1 below for a brief overview.

Albeit the effectiveness and success of the kernel-spectral methods in many applications, these methods are usually applied haphazardly, especially in terms of tuning parameter selection and interpretation of the results. For example, as a key step in these methods, the construction of the kernel (or affinity) matrices requires specifying a proper bandwidth parameter, which is commonly determined by unjustified heuristics or conventional empiricism. This is mainly due to a lack of theoretical understanding of the methods, including its intrinsic objective, its range of applicability, and its susceptibility to noise or dimensionality of the data. Likewise, the absence of a theoretical foundation may significantly constrain the users’ recognition or exploitation of the full potentials of the method. Given the indispensable status and the practical power of these methods in many fields of applications, such as single-cell transcriptomics [72, 49, 41] and medical informatics [1, 59], there is a pressing need of theoretically justified kernel-spectral method that accounts for both the high-dimensionality and the noisiness of the data.

In this study, we focus on an integral operator approach to learning low-dimensional nonlinear structures from high-dimensional noisy data. We propose a kernel-spectral embedding algorithm with a data-adaptive bandwidth selection procedure (c.f. Algorithm 1), justified by rigorous theoretical analysis, and provide solid interpretations of the low-dimensional embeddings by establishing its asymptotic behaviors in the large system limit.

Specifically, we consider the following manifold “signal-plus-noise” data-generative model

$$\mathbf{y}_i = \mathbf{x}_i + \mathbf{z}_i \in \mathbb{R}^p, \quad 1 \leq i \leq n, \quad (1.1)$$

where $\{\mathbf{y}_i\}_{1 \leq i \leq n}$ are observed samples, $\{\mathbf{x}_i\}_{1 \leq i \leq n}$ are the underlying noiseless samples drawn independently from a low-dimensional smooth manifold \mathcal{M} of interest, embedded into \mathbb{R}^p , and $\{\mathbf{z}_i\}_{1 \leq i \leq n}$ are independent sub-Gaussian noise (see Section 1.3 for the definition) with covariance $\sigma^2 \mathbf{I}$. As will be seen in Section 3.1, (1.1) is closely related to the spiked covariance model [37] extensively studied in the past two decades. Throughout, we focus on the high-dimensional setting where the number of variables p is comparable to the sample size n , that is, for some constant $0 < \tau < 1$, we have

$$\tau \leq \frac{n}{p} \leq \tau^{-1}. \quad (1.2)$$

As a general and important problem in nonlinear dimension reduction and manifold learning, our goal is to find a well-justified low-dimensional embedding of $\{\mathbf{y}_i\}_{1 \leq i \leq n}$ that captures the nonlinear structure of the underlying manifold \mathcal{M} , as encapsulated in the noiseless random samples $\{\mathbf{x}_i\}_{1 \leq i \leq n}$. To facilitate our discussion, we define the Gaussian kernel matrix $\mathbf{K}_n \in \mathbb{R}^{n \times n}$, where

$$\mathbf{K}_n = (K(i, j))_{1 \leq i, j \leq n}, \quad K(i, j) = \exp\left(-\frac{\|\mathbf{y}_i - \mathbf{y}_j\|_2^2}{h_n}\right), \quad (1.3)$$

and $h_n > 0$ is some bandwidth.

1.1 Some Related Works

Unlike our general setup (1.1) under high-dimensionality (1.2), most of the existing work concern computational algorithms for learning nonlinear manifold \mathcal{M} from random observations based on heuristics developed

under either the noiseless (i.e., $\mathbf{y}_i = \mathbf{x}_i$) or low-dimensional settings where p is fixed. These methods can be roughly separated into two categories, depending on how the data is conceptually represented. On the one hand, there are spectral graph based methods, including Laplacian eigenmap [6], diffusion map (DM) [19], vector diffusion map (VDM) [61], ISOMAP [66], maximal variance unfolding (MVU) [73], locally linear embedding (LLE) [53], Hessian LLE [23], t-SNE [67], UMAP [48] and local tangent space alignment (LTSA) [76], among many others. For more details of these methods, see [44, 68]. Generally speaking, these methods start by constructing a possibly sparse graph using kernels in which the nodes represent the input patterns and the edges represent the neighborhood relations. Consequently, the resulting graph can be viewed as a discretized approximation of \mathcal{M} sampled by the inputs. From these graphs, one may apply results from spectral graph theory and construct matrices whose spectral decomposition reveals the low-dimensional structure of \mathcal{M} . Incidentally, these methods have been used to facilitate various downstream statistical applications, such as spectral clustering [69], regression analysis [17], among others. The main differences between these methods are the kernels used to construct the spectral graphs and the associated nonlinear eigenfunctions (or feature maps [34]) employed for embedding (or data representation). On the other hand, there are reproducing kernel Hilbert space (RKHS) based methods, that use eigenfunctions of some kernel map of the RKHS to infer the nonlinear structures of \mathcal{M} based on noiseless observations [56, 34, 43]. Specifically, these methods start from a certain similarity matrix based on some positive kernel function, and infer the geometric properties from the integral operator associated with the kernel. Similarly, various downstream tasks such as clustering, regression and classification [34, 54, 58, 70] have been treated in combination with the RKHS-based methods. In addition to the above two categories, kernel principal component analysis (kPCA) [55] has also been widely used.

From a mathematical viewpoint, in the low-dimensional and noiseless setting, theoretical properties of some of these methods have been explored. For the graph-based methods, existing theoretical results reveal that, under some regularity conditions, the discretized approximation obtained from various kernel-spectral methods will converge to a continuum quantity, which is usually represented as a certain operator capturing the underlying structures of \mathcal{M} . For example, it has been shown that the discrete Graph Laplacian (GL) matrices (c.f. (2.6) and (2.7)) used by Laplacian eigenmap and DM would converge to the Laplace-Beltrami operator of \mathcal{M} under various settings and assumptions [7, 15, 24, 31, 32, 60, 62, 74]. For the LLE, as shown in [75], after being properly normalized, the similarity matrix would converge to the LLE kernel which is closely related to the Laplace-Beltrami operator. Convergence of t-SNE, MVU, VDM and LTSA have been studied in [4, 45, 14, 3, 61, 65]. For the RKHS-based methods, it has been shown that the empirical eigenvalues and eigenfunctions would converge to those of the integral operator associated with the reproducing kernel [13, 42, 51, 58, 63, 64, 70]. Finally, kPCA has been studied under the noiseless setting [10].

Another important difference between the graph-based methods and the RKHS-based methods lie in the treatment of the kernel matrices (c.f. (1.3)). The graph-based methods usually rely on some GL-type operations, where the kernel (affinity) matrix are properly normalized by the graph degrees [20, 68]. In contrast, the RKHS-based methods commonly employ the kernel matrix directly without further normalization. Consequently, in terms of interpretations, existing theory under the low-dimensional noiseless setting indicate that the embeddings from the graph-based methods are associated with the eigenfunctions of Laplace-Beltrami operator of \mathcal{M} , whereas those from the RKHS-based methods are related to the eigenfunctions of some reproducing kernels of \mathcal{M} .

Albeit these endeavors, much less is known when the data is high-dimensional and noisy as modeled by (1.1) and (1.2), nor does the behavior of the associated kernel random matrix \mathbf{K}_n . In the null case (i.e., $\mathbf{y}_i = \mathbf{z}_i$), it has been shown in [11, 18, 21, 22, 26, 29] that when $h_n = p$, the random kernel matrix \mathbf{K}_n can be well approximated by a low-rank perturbed random Gram matrix. Consequently, studying \mathbf{K}_n under pure noise is closely related to PCA with some low-rank perturbations. Moreover, since in this case the

degree matrix is close to a scalar matrix [21], the graph-based methods and the RKHS-based methods are asymptotically equivalent. As for the non-null cases, spectral convergence of \mathbf{K}_n has been studied in some special cases in [25] when $h_n = p$, and more recently under a general setting in [20]. These results show how the eigenvalues of the kernel matrices of $\{\mathbf{y}_i\}_{1 \leq i \leq n}$ relate to those of $\{\mathbf{x}_i\}_{1 \leq i \leq n}$. Moreover, as can be seen in [20], in the non-null cases, the degree matrix is usually non-trivial, so that the graph-based methods can be very different from the RKHS-based methods.

In what follows, we focus on an RKHS-based integral operator approach to nonlinear dimension reduction and manifold learning under the general setup (1.1) and (1.2). Even though in this setting \mathbf{K}_n has been studied to some extent in [20, 25], several pieces are still missing for rigorous and interpretable statistical applications. Firstly, it is unclear how to select the bandwidth adaptively for embedding, that is, free from prior knowledge of \mathcal{M} . Secondly, the limiting behavior of the eigenvectors of \mathbf{K}_n have not been analyzed. Such results are particularly relevant for embedding purposes. Finally, even though the convergence of kernel matrices associated to $\{\mathbf{y}_i\}_{1 \leq i \leq n}$ (c.f. (1.3)) and $\{\mathbf{x}_i\}_{1 \leq i \leq n}$ (c.f. (3.5)) can be established, it is unclear how they are related to the underlying manifold \mathcal{M} . Such results are important for appropriate interpretations of the embeddings. We will accomplish these goals in this paper.

1.2 An Overview of Main Results and Contributions

Briefly speaking, our proposed kernel-spectral embedding algorithm starts by constructing a Gaussian kernel matrix $\mathbf{K}_n \in \mathbb{R}^{n \times n}$ as defined in (1.3), where h_n is carefully selected by a theory-guided data-adaptive procedure proposed in Section 2. Then we obtain the kernel-spectral embedding of the original data $\{\mathbf{y}_i\}_{1 \leq i \leq n}$ by conducting an eigen-decomposition for the scaled kernel matrix $\frac{1}{n}\mathbf{K}_n$, and define the embeddings as the leading eigenvectors of $\frac{1}{n}\mathbf{K}_n$, weighted by their associated eigenvalues (Algorithm 1). As we will show later, as $(n, p) \rightarrow \infty$ with respect to (1.2), the thus constructed final embeddings are essentially related to and determined by a population integral operator defined by the reproducing kernel of an RKHS associated to the underlying manifold \mathcal{M} . It is in this sense our proposed method is an integral operator approach.

Rigorous theoretical understanding are obtained for the proposed algorithm, including the theoretical justifications for the bandwidth selection procedure, the limiting behavior of the low-dimensional embeddings, and their interpretations in relation to the underlying manifolds. Compared to the existing works on kernel-spectral embeddings (see Section 1.1), the current study has the following methodological advantages and theoretical significance:

- We propose a kernel-spectral embedding algorithm for learning low-dimensional nonlinear structure from high-dimensional noisy data. Unlike most existing methods, our proposal takes into account both the noisiness of the data, characterized by our model (1.1), and its high-dimensionality as in (1.2). To the best of our knowledge, this is the first kernel-spectral embedding method with theoretically guaranteed performance for high-dimensional and noisy data under the non-null settings.
- A key component in any kernel-based method is to select a proper bandwidth parameter. One major innovation of our proposed method lies in a careful analysis of the asymptotic behavior of kernel random matrices constructed from high-dimensional noisy data, which in turn leads to a theory-informed bandwidth selection procedure guaranteeing the strong performance of the method in a data-adaptive manner. In particular, our bandwidth selection procedure does not rely on prior knowledge about the underlying manifold, and can be implemented efficiently.
- We also provide in-depth theoretical understanding of the proposed method. On the one hand, we study the convergence of the final low-dimensional embeddings to their oracle counterparts based on

the noiseless samples $\{\mathbf{x}_i\}_{1 \leq i \leq n}$ in the large system limit, and characterize explicitly the effect of the underlying signal-to-noise ratio on the respective rates of convergence and phase transition. On the other hand, we establish the convergence of the kernel matrices to the population integral operator that captures the intrinsic geometry of the underlying manifold. The second result is essential for our understanding of the final low-dimensional embeddings, interpreted as a finite approximation of the samples projected onto the leading eigenfunctions of the population integral operator.

Our theoretical results explain the empirically observed data-adaptive nature of the proposed method (Section 4), which extracts the nonlinear structure from the data regardless which kind of manifold is in play. Moreover, our recognition of the limiting integral operator also suggests potential advantages of our method over alternative approaches targeting for distinct geometric features of the manifold. For example, we may conclude from the theory that our method differs significantly from the graph-based methods, such as Laplacian eigenmap, DM, and LLE, as they all essentially aim at the Laplace-Beltrami operator rather than an integral operator (see Sections 2.2 and 5 for more discussions).

Our theoretical analysis, on the one hand, relies on a general model reduction scheme, detailed in Section 3.1, which simplifies the analysis by connecting the noisy manifold model (1.1) with a spiked covariance model. On the other hand, we also leverage advanced tools from operator theory such as the theory of RKHS and random matrix theory, to prove our main results.

The proposed method admits strong empirical performance. In Section 4.1, we present simulation studies that show the superiority and flexibility of the proposed bandwidth selection method over some existing alternatives. In Section 4.2, we analyze three real-world high-dimensional datasets with distinct nonlinear structures, including a path manifold, a circle manifold, and a multiclass mixture manifold, to demonstrate the usefulness of the method. In particular, for each of the examples, our proposed method shows significant improvements over the existing state-of-the-art methods in inferring the respective underlying nonlinear structures.

1.3 Organization and Notations

The rest of the paper is organized as follows. In Section 2, we introduce our proposed kernel-spectral embedding algorithm in detail, and we point out important differences between our proposal and some existing methods. In Section 3, we study the theoretical properties of the proposed method, including the convergence of the low-dimensional embeddings to its noiseless counterpart, and the spectral convergence of the kernel matrix to an integral operator. In Section 4, we include our simulation studies on bandwidth selection and analyze three real-world datasets to show the numerical performance of the proposed method in various applications. Finally, we discuss some extensions and related problems in Section 5. Technical proofs and additional discussions and numerical results are provided in Appendices A–D.

We will finish this section by introducing some notations used in the paper. To streamline our statements, we use the notion of stochastic domination, which is commonly adopted in advanced probability theory to syntactically simplify precise statements of the form “ $\mathbf{X}^{(n)}$ is bounded with high probability by $\mathbf{Y}^{(n)}$ up to small powers of n .”

Definition 1.1 (Stochastic domination). *Let*

$$\mathbf{X} = \{\mathbf{X}^{(n)}(u) : n \in \mathbb{N}, u \in \mathbf{U}^{(n)}\}, \quad \mathbf{Y} = \{\mathbf{Y}^{(n)}(u) : n \in \mathbb{N}, u \in \mathbf{U}^{(n)}\},$$

be two families of nonnegative random variables, where $\mathbf{U}^{(n)}$ is a possibly n -dependent parameter set. We say that \mathbf{X} is stochastically dominated by \mathbf{Y} , uniformly in the parameter u , if for all small $v > 0$ and large

$D > 0$, there exists $n_0(v, D) \in \mathbb{N}$ so that we have

$$\sup_{u \in \mathcal{U}^{(n)}} \mathbb{P}\left(\mathbf{X}^{(n)}(u) > n^v \mathbf{Y}^{(n)}(u)\right) \leq n^{-D},$$

for all $n \geq n_0(v, D)$. In addition, we say that an n -dependent event $\Omega \equiv \Omega(n)$ holds with high probability if for any large $D > 1$, there exists $n_0 = n_0(D) > 0$ so that

$$\mathbb{P}(\Omega) \geq 1 - n^{-D},$$

for all $n \geq n_0$.

We interchangeably use the notation $\mathbf{X} = \mathcal{O}_{\prec}(\mathbf{Y})$, $\mathbf{X} \prec \mathbf{Y}$ or $\mathbf{Y} \succ \mathbf{X}$ if \mathbf{X} is stochastically dominated by \mathbf{Y} , uniformly in $u \in \mathcal{U}^{(n)}$, when there is no risk of confusion. For two sequences of deterministic positive values $\{a_n\}$ and $\{b_n\}$, we write $a_n = \mathcal{O}(b_n)$ if $a_n \leq Cb_n$ for some positive constant $C > 0$. In addition, if both $a_n = \mathcal{O}(b_n)$ and $b_n = \mathcal{O}(a_n)$, we write $a_n \asymp b_n$. Moreover, we write $a_n = o(b_n)$ if $a_n \leq c_n b_n$ for some positive sequence $c_n \rightarrow 0$. For any probability measure \mathbb{P} over Ω , we denote $\mathcal{L}_2(\Omega, \mathbb{P})$ as the collection of L_2 -integrable functions with respect to \mathbb{P} , that is, for any $f \in \mathcal{L}_2(\Omega, \mathbb{P})$, we have $\|f\|_{\mathbb{P}} = \sqrt{\int_{\Omega} |f(y)|^2 \mathbb{P}(dy)} < \infty$. For a vector $\mathbf{a} = (a_1, \dots, a_n)^{\top} \in \mathbb{R}^n$, we define its ℓ_p norm as $\|\mathbf{a}\|_p = \left(\sum_{i=1}^n |a_i|^p\right)^{1/p}$. We denote $\text{diag}(a_1, \dots, a_n) \in \mathbb{R}^{n \times n}$ as the diagonal matrix whose i -th diagonal entry is a_i . For a matrix $\mathbf{A} = (a_{ij}) \in \mathbb{R}^{n \times n}$, we define its Frobenius norm as $\|\mathbf{A}\|_F = \sqrt{\sum_{i=1}^n \sum_{j=1}^n a_{ij}^2}$, and its operator norm as $\|\mathbf{A}\| = \sup_{\|\mathbf{x}\|_2 \leq 1} \|\mathbf{A}\mathbf{x}\|_2$. For any integer $n > 0$, we denote the set $[n] = \{1, 2, \dots, n\}$. For a random vector \mathbf{g} , we say it is sub-Gaussian if

$$\mathbb{E} \exp(\mathbf{a}^{\top} \mathbf{g}) \leq \exp\left(\|\mathbf{a}\|_2^2/2\right), \quad (1.4)$$

for any deterministic vector \mathbf{a} . Throughout, C, C_1, C_2, \dots are universal constants independent of n , and can vary from line to line.

2 Kernel-Spectral Embedding for High-Dimensional Noisy Data

In this section, we introduce in detail our proposed bandwidth selection and kernel-spectral embedding algorithm. After that we discuss its unique features compared with some popular existing methods.

2.1 Data-Adaptive Embedding Algorithm

Our proposed embedding method is summarized as Algorithm 1 below.

In Step 1 of the algorithm, a data-adaptive bandwidth parameter h_n is defined as the ω -percentail of the empirical cumulative distribution function $\nu_n(t)$ of the pairwise squared-distances $\{d_{ij}\}_{1 \leq i < j \leq n}$ among the observed data. Such a strategy is motivated by our theoretical analysis of the spectrum of kernel random matrices and its dependence on the associated bandwidth parameter. It ensures the thus determined bandwidth h_n adapts well to the unknown manifold structure and the signal-to-noise ratio of the data, so that the associated kernel matrix captures the respective underlying low-dimensional structure via an integral operator. ω is a tunable parameter. In Section 3, we show in theory that ω can be chosen as any constant between 0 and 1 to have the final embeddings achieve the same asymptotic behavior; in Section 4, we also demonstrate numerically that the final embeddings are insensitive to the choice of ω . In practice,

Algorithm 1 High-dimensional noisy kernel-spectral embedding

Input: Observed samples $\{\mathbf{y}_i\}_{i \in [n]}$, $\omega \in (0, 1)$ and $\Omega \subseteq \{1, 2, \dots, n\}$.

1. **Bandwidth selection:**

(i) let $d_{ij} = \|\mathbf{y}_i - \mathbf{y}_j\|_2^2$ for all $1 \leq i < j \leq n$, and denote

$$\nu_n(t) = \frac{2}{n(n-1)} \sum_{1 \leq i < j \leq n} 1_{\{d_{ij} \leq t\}}, \quad (2.1)$$

(ii) define the bandwidth h_n to be the solution to the equation

$$\nu_n(h) = \omega. \quad (2.2)$$

2. **Kernel matrix construction:** define the kernel matrix $\mathbf{K}_n = (K(i, j))_{1 \leq i, j \leq n}$ using the above bandwidth h_n by letting

$$K(i, j) = \exp\left(-\frac{\|\mathbf{y}_i - \mathbf{y}_j\|_2^2}{h_n}\right). \quad (2.3)$$

3. **Spectral embedding:**

(i) obtain the eigendecomposition of the scaled kernel matrix $n^{-1}\mathbf{K}_n$ as

$$\frac{1}{n}\mathbf{K}_n = \mathbf{U}\mathbf{\Lambda}\mathbf{U}^\top, \quad (2.4)$$

where $\mathbf{\Lambda} = \text{diag}(\lambda_1, \lambda_2, \dots, \lambda_n) \in \mathbb{R}^{n \times n}$ with $\lambda_1 \geq \lambda_2 \geq \dots \geq \lambda_n$ being the eigenvalues of $n^{-1}\mathbf{K}_n$, and $\mathbf{U} = [\mathbf{u}_1 \ \mathbf{u}_2 \ \dots \ \mathbf{u}_n] \in \mathbb{R}^{n \times n}$ with $\{\mathbf{u}_i\}_{1 \leq i \leq n}$ being the corresponding eigenvectors.

(ii) define the kernel-spectral embeddings as the rows of $\mathbf{U}_\Omega \mathbf{\Lambda}_\Omega \in \mathbb{R}^{n \times |\Omega|}$, where $\mathbf{U}_\Omega \in \mathbb{R}^{n \times |\Omega|}$ and $\mathbf{\Lambda}_\Omega \in \mathbb{R}^{|\Omega| \times |\Omega|}$ only contain the eigenvectors and eigenvalues indexed by elements in Ω .

Output: the embedding matrix $\mathbf{U}_\Omega \mathbf{\Lambda}_\Omega \in \mathbb{R}^{n \times |\Omega|}$.

to optimize the empirical performance and improve automation of the method, we recommend using a resampling approach, described in Appendix D, to determine ω .

In Step 2, the Gaussian kernel is adopted for the construction of kernel matrices. This is mainly due to its wide use in practice and the relative simplicity of its theoretical analysis, although other kernel functions may be considered in practice (see Section 5 for more discussions).

In Step 3, the final embeddings are defined as the Ω -indexed leading eigenvectors of the scaled kernel matrix, weighted by their eigenvalues. Similar forms of embeddings have been considered in [2] for spectral clustering and in [77] for network clustering. The coordinate set Ω of the embedding space is determined by the users, depending on the specific aims or downstream applications of the low-dimensional embeddings. For example, in Section 4.2, we choose $\Omega = \{1, 2\}$ for visualizing a path manifold, and $\Omega = \{2\}$ for the downstream ranking task, choose $\Omega = \{2, 3\}$ for learning circle manifolds, and set $\Omega = \{1, 2, \dots, r\}$ for a variety of integers r for downstream clustering purposes.

2.2 Comparison with Existing Kernel-Spectral Embedding Methods

Regardless of the kernel functions being used, Algorithm 1 has important differences from the existing kernel-spectral embedding methods. We first focus on kPCA, Laplacian eigenmap, and DM due to their

close relations to our proposal.

Compared to Step 3 of Algorithm 1, these methods rely on eigendecomposition of matrices distinct from $n^{-1}\mathbf{K}_n$. Specifically, in the standard kPCA implementation (Section 12.3 of [9]), the eigendecomposition is applied to the centred kernel matrix

$$\bar{\mathbf{K}}_n = \mathbf{K}_n - \frac{1}{n}\mathbf{1}\mathbf{1}^\top\mathbf{K}_n - \frac{1}{n}\mathbf{K}_n\mathbf{1}\mathbf{1}^\top + \frac{1}{n^2}\mathbf{1}\mathbf{1}^\top\mathbf{K}_n\mathbf{1}\mathbf{1}^\top, \quad (2.5)$$

where $\mathbf{1} \in \mathbb{R}^n$ is an all-one vector; in Laplacian eigenmap [6], the eigendecomposition is applied to the kernelized graph Laplacian matrix

$$\mathbf{L}_n = \mathbf{I} - \mathbf{D}_n^{-1}\mathbf{K}_n, \quad (2.6)$$

where $\mathbf{D}_n = \text{diag}(\sum_{j=1}^n K(1, j), \dots, \sum_{j=1}^n K(n, j))$; in diffusion map [19], the eigendecomposition is applied to the normalized kernel matrix (i.e., transition matrix)

$$\mathbf{M}_n = \mathbf{D}'_n^{-1}\mathbf{K}'_n, \quad \mathbf{K}'_n = \mathbf{D}_n^{-\zeta}\mathbf{K}_n\mathbf{D}_n^{-\zeta}, \quad (2.7)$$

where $\zeta > 0$ is some tunable parameter and $\mathbf{D}'_n = \text{diag}(\sum_{j=1}^n K'(1, j), \dots, \sum_{j=1}^n K'(n, j))$. More importantly, our numerical results (Section 4.2) indicate that such differences may lead to distinct low-dimensional embeddings, which, according to our theory (Section 3.3), may correspond to geometric features of the underlying manifold, that are identifiable by the proposed method but not likely to be captured by these methods.

As for other existing methods, it is largely unclear to what extent their performance is guaranteed, or if their interpretations continue to hold, for general high-dimensional and noisy datasets. Empirically, our real applications in Sections 4.2.2 and 4.2.3 show that our proposed method outperforms various existing methods, especially when dimension increases (Figure 4).

Moreover, compared to the existing methods, Algorithm 1 has a bandwidth selection procedure that is provably coherent with the subsequent steps, in the sense that both the high-dimensionality and noisiness of the data are intrinsically accounted for in the constructed kernel matrix and the final embeddings. In contrast, graph-based methods usually require the bandwidth decrease to zero, to ensure a meaningful convergence. However, oftentimes this is not admissible under high-dimensional and noisy datasets. In this respect, we are only aware of the recent work [20], in which a data-driven bandwidth selection procedure for GL was developed. Nonetheless, in Section 4, we compare various bandwidths and demonstrate the advantage of the proposed bandwidth; we also show that, even after incorporating the proposed bandwidth to these existing methods, Algorithm 1 still has the superior performance in learning low-dimensional structures from the real-world datasets.

3 Theoretical Properties: Justifications and Interpretations

We develop a theoretical framework to rigorously justify the embedding algorithm proposed in Section 2.1. Consequently, our theory suggests an asymptotic geometric interpretation that helps to better understand the final low-dimensional embeddings.

3.1 General Model Reduction Scheme

To facilitate our analysis of the proposed embedding algorithm under model (1.1), we introduce a useful model reduction scheme, that significantly simplifies the theoretical analysis without sacrificing the generality of our discussions.

Suppose the underlying manifold $\mathcal{M} \subseteq \mathbb{R}^p$ is m -dimensional. By Nash's isometric embedding theorem [50], there exists some integer $r \leq \frac{m(3m+11)}{2}$ so that the embedded manifold is supported in an r -dimensional subspace in \mathbb{R}^p . Consequently, there exists a deterministic rotation matrix $\mathbf{R} \in \mathbb{R}^{p \times p}$ only depending on \mathcal{M} such that

$$\mathbf{R}\mathbf{x}_i = (x_{i1}, x_{i2}, \dots, x_{ir}, 0, \dots, 0)^\top \in \mathbb{R}^p.$$

Now suppose $\{\mathbf{x}_i\}_{1 \leq i \leq n}$ are drawn independently from a probability measure on \mathcal{M} . Let $\mathbf{\Sigma}$ be the covariance matrix of $(x_{i1}, x_{i2}, \dots, x_{ir})^\top$, and denote its eigendecomposition as

$$\mathbf{\Sigma} = \mathbf{V}\mathbf{\Gamma}\mathbf{V}^\top,$$

where $\mathbf{\Gamma} = \text{diag}(\theta_1, \dots, \theta_r)$ contains the eigenvalues of $\mathbf{\Sigma}$, arranged in nonincreasing order, and the columns of $\mathbf{V} \in \mathbb{R}^{r \times r}$ are the corresponding eigenvectors. Given \mathbf{V} , we could define an orthonormal matrix $\mathbf{O} \in \mathbb{R}^{p \times p}$ as

$$\mathbf{O} = \begin{pmatrix} \mathbf{V}^\top & \mathbf{0} \\ \mathbf{0} & \mathbf{I}_{p-r} \end{pmatrix}.$$

Then it is clear that for each $i \in [n]$, the covariance matrix of $\mathbf{O}\mathbf{R}\mathbf{x}_i$ is diagonal, with

$$\text{Cov}(\mathbf{O}\mathbf{R}\mathbf{x}_i) = \begin{pmatrix} \mathbf{\Gamma} & \mathbf{0} \\ \mathbf{0} & \mathbf{0} \end{pmatrix}. \quad (3.1)$$

Therefore, by rotating the original model (1.1) with a deterministic matrix $\mathbf{O}\mathbf{R}$, we obtain that

$$\mathbf{y}_i^0 = \mathbf{x}_i^0 + \mathbf{z}_i^0, \quad (3.2)$$

where $\mathbf{y}_i^0 = \mathbf{O}\mathbf{R}\mathbf{y}_i$, $\mathbf{x}_i^0 = \mathbf{O}\mathbf{R}\mathbf{x}_i$ and $\mathbf{z}_i^0 = \mathbf{O}\mathbf{R}\mathbf{z}_i$. In particular, after rotation $\{\mathbf{x}_i^0\}_{1 \leq i \leq n}$ become independent sparse random vectors in the sense that

$$\mathbf{x}_i^0 = (\mathbf{x}_i^0, 0, \dots, 0) \in \mathbb{R}^p, \quad (3.3)$$

where $\mathbf{x}_i^0 = (x_{i1}^0, \dots, x_{ir}^0) \in \mathbb{R}^r$ and

$$\text{Cov}(\mathbf{x}_i^0) = \mathbf{\Gamma} = \text{diag}(\theta_1, \dots, \theta_r), \quad (3.4)$$

whereas the random noises $\{\mathbf{z}_i^0\}_{1 \leq i \leq n}$ remains independent and centred. Now a key observation is that the kernel matrix \mathbf{K}_n from (2.3) only depends on the pairwise Euclidean distances of the data $\{\mathbf{y}_i\}_{1 \leq i \leq n}$, which are invariant to any rotations. In other words, we have

$$\exp\left(-\frac{\|\mathbf{y}_i - \mathbf{y}_j\|_2^2}{h}\right) = \exp\left(-\frac{\|\mathbf{y}_i^0 - \mathbf{y}_j^0\|_2^2}{h}\right), \quad 1 \leq i, j \leq n.$$

Therefore, to theoretically analyze the kernel random matrix \mathbf{K}_n and the subsequent spectral embeddings, we can invariably start from the structurally reduced model as characterized by (3.2) to (3.4).

The main benefit of such a reduction scheme is two-fold. On the one hand, it helps to identify a natural coordinate system for the noiseless samples $\{\mathbf{x}_i\}_{1 \leq i \leq n}$ so that the underlying low-dimensional manifold only relies on their first few nonzero coordinates. On the other hand, the reparametrization leads to a parsimonious model in which the sampling distribution from the underlying manifold has a simple diagonal covariance structure. Both aspects contribute to improving the theoretical accessibility of the problem without loss of generality.

3.2 Spectral Convergence to Noiseless Kernel Matrix

In this part, we show the convergence of the low-dimensional embeddings to their noiseless counterparts, by establishing the spectral convergence of the scaled kernel random matrix $n^{-1}\mathbf{K}_n$ to the noiseless random matrix $n^{-1}\mathbf{K}_n^*$, defined by

$$\mathbf{K}_n^* = (K^*(i, j))_{1 \leq i, j \leq n}, \quad K^*(i, j) = \exp\left(-\frac{\|\mathbf{x}_i - \mathbf{x}_j\|_2^2}{h}\right), \quad (3.5)$$

where $h = \sum_{i=1}^r \theta_i + p\sigma^2$ with σ^2 being the noise level as in (3.6).

By the invariance $\|\mathbf{x}_i - \mathbf{x}_j\|_2 = \|\mathbf{x}_i^0 - \mathbf{x}_j^0\|_2$, the noiseless kernel matrix \mathbf{K}_n^* can also be treated as a characterization of the noiseless samples embedded in \mathbb{R}^r . To this end, we first introduce and discuss the theoretical assumptions we made throughout our analysis.

Assumption 3.1. *We assume that both $\{\mathbf{x}_i\}_{1 \leq i \leq n}$ and $\{\mathbf{z}_i\}_{1 \leq i \leq n}$ in (1.1) are independent sub-Gaussian random vectors, and*

$$\mathbb{E}\mathbf{z}_i = 0, \quad \text{Cov}(\mathbf{z}_i) = \sigma^2 \mathbf{I}_p, \quad (3.6)$$

with $\sigma^2 \asymp n^\beta$ for some constant $\beta \geq 0$. Moreover, in the reduced model (3.2) to (3.4), we assume that

$$r \equiv r(n) = O(\log^c n), \quad (3.7)$$

for some constant $c \geq 0$, and for all $1 \leq i \leq r$,

$$\theta_i \asymp n^\alpha, \quad (3.8)$$

for some constant $\alpha \geq 0$.

A few remarks on Assumption 3.1 are in order. First, unlike most of the existing literature on manifold learning and random matrix theory where r is usually assumed to be bounded, our assumption (3.7) allows r to diverge slowly with n . This is more flexible for practical applications and it guarantees that the bandwidth selected according to (2.2) has the same order as the signal (i.e., $\sum_{i=1}^r \theta_i$) with high probability. Second, for ease of statements, we assume that (3.8) holds for the same α . However, our results can easily generalize to the setting $\theta_i \asymp n^{\alpha_i}$ for some nonnegative constants $\{\alpha_i\}_{1 \leq i \leq r}$, with some minor adaptation of our argument and extra notational complications. Finally, in the current paper, we assume that $\{\mathbf{z}_i\}_{1 \leq i \leq n}$ and therefore $\{\mathbf{z}_i^0\}_{1 \leq i \leq n}$ are white noise as in (3.6) for simplicity. Nevertheless, our discussion applies invariably to the colored noise setting where $\text{Cov}(\mathbf{z}_i)$ has the same eigenspace as $\text{Cov}(\mathbf{x}_i)$. For example, in light of (3.4), we can allow a diagonal but non-scalar covariance matrix for $\text{Cov}(\mathbf{z}_i^0)$.

Before stating the main result of this part, we introduce a few more notations. We denote the eigenvalues of $n^{-1}\mathbf{K}_n^*$ as $\{\mu_i\}_{1 \leq i \leq n}$ where $\mu_1 \geq \mu_2 \geq \dots \geq \mu_n$, and denote the corresponding eigenvectors as $\{\mathbf{v}_i\}_{1 \leq i \leq n}$. Let \mathbf{P} be the probability measure on \mathbb{R}^r for the independent subvectors $\{\mathbf{x}_i^0\}_{1 \leq i \leq n}$ of the reduced noiseless samples $\{\mathbf{x}_i^0\}_{1 \leq i \leq n}$. We define the associated integral operator \mathcal{K} such that, for any $f \in \mathcal{L}_2(\mathbb{R}^r, \mathbf{P})$, we have

$$\mathcal{K}f(\mathbf{x}) = \int \exp\left(-\frac{\|\mathbf{x} - \mathbf{y}\|_2^2}{h}\right) f(\mathbf{y}) \mathbf{P}(d\mathbf{y}), \quad \mathbf{x}, \mathbf{y} \in \mathbb{R}^r. \quad (3.9)$$

By Mercer's theorem (e.g., [39]), there exist a sequence of nonnegative eigenvalues $\{\gamma_i\}_{i \geq 1}$ in the decreasing order and orthonormal basis of $\mathcal{L}_2(\mathbb{R}^r, \mathbf{P})$, known as eigenfunctions so that

$$\mathcal{K}\phi_i(\mathbf{x}) = \gamma_i \phi_i(\mathbf{x}), \quad \text{for } i \geq 1. \quad (3.10)$$

Finally, we also recall that the eigenvalues and eigenvectors of $n^{-1}\mathbf{K}_n$ are denoted as $\{\lambda_i\}_{1 \leq i \leq n}$ and $\{\mathbf{u}_i\}_{1 \leq i \leq n}$, respectively.

Theorem 3.2. *Suppose Assumption 3.1 holds and $\alpha > \beta + 1$. Then the following holds.*

1. (Eigenvalue convergence) *We have*

$$\|n^{-1}\mathbf{K}_n - n^{-1}\mathbf{K}_n^*\| = O_{\prec} \left(\frac{1}{\sqrt{n}} + \frac{1}{rn^{\alpha-\beta-1}} \right), \quad (3.11)$$

and therefore

$$\max_{i \in [n]} |\lambda_i - \mu_i| = O_{\prec} \left(\frac{1}{\sqrt{n}} + \frac{1}{rn^{\alpha-\beta-1}} \right).$$

2. (Eigenvector convergence) *For any $i \in [n]$, if the i -th population eigen-gap*

$$r_i := \min\{\gamma_{i-1} - \gamma_i, \gamma_i - \gamma_{i+1}\}, \quad (3.12)$$

satisfies that for some fixed constant $\epsilon > 0$ and some constant $C > 0$

$$r_i^2 \geq Cn^\epsilon \left(\frac{1}{\sqrt{n}} + \frac{1}{rn^{\alpha-\beta-1}} \right), \quad (3.13)$$

then we have

$$|\langle \mathbf{u}_i, \mathbf{v}_i \rangle^2 - 1| = O_{\prec} \left(\left[\frac{1}{\sqrt{n}} + \frac{1}{rn^{\alpha-\beta-1}} \right] \frac{1}{r_i^2} \right). \quad (3.14)$$

Theorem 3.2 establishes the asymptotic spectral equivalence between the noisy kernel matrix $n^{-1}\mathbf{K}_n$ and the noiseless kernel matrix $n^{-1}\mathbf{K}_n^*$. Note that both matrices are random with respect to the underlying manifold and noise. We provide several remarks here. First, unlike many existing results on the spectral convergence of kernel random matrices, Theorem 3.2 reveals the role of r in the convergence rate, suggesting that when r does not diverge fast, a larger r will potentially lead to a faster convergence between the two matrices. Second, as shown in Corollary 3.2 of [20], for $i \gg \log n$, we have $\mu_i = O_{\prec}(n^{-1})$. Consequently, in practice, we only need to focus on recovering the first few (at most at an order of $\log n$) eigenvalues and eigenvectors of $n^{-1}\mathbf{K}_n^*$. Third, the results concerning r_i can be made more precise given additional information. For example, if \mathbf{P} is Gaussian and $\sigma = 1$, then from Appendix C, for any finite i , we have $r_i \asymp 1$. In this case, whenever $\alpha > 3/2$, we have \sqrt{n} -consistency for the leading $N = O(1)$ eigenvalues and eigenvectors

$$\max_{i \in [N]} |\lambda_i - \mu_i| = O_{\prec}(n^{-1/2}),$$

and

$$\max_{i \in [N]} \|\mathbf{u}_i - \mathbf{v}_i\|_2^2 = 2 - 2 \min_{i \in [n]} \langle \mathbf{u}_i, \mathbf{v}_i \rangle^2 = O_{\prec}(n^{-1/2}).$$

Remark 3.3. We point out that our assumption on the signal-to-noise ratio $\alpha > \beta + 1$ is actually necessary to guarantee convergence. As proved in part (i) of Theorem 3.1 of [20], when $\alpha < \beta + 1$, the noise dominates the signal and the convergence between $n^{-1}\mathbf{K}_n$ and $n^{-1}\mathbf{K}_n^*$ fails to hold. Indeed, if $\sigma = 1$ and $\alpha < 1$, we have $h_n \asymp p$, so that asymptotically $n^{-1}\mathbf{K}_n$ can be approximated by the Gram matrix of the noise vectors $\{\frac{1}{\sqrt{n}}\mathbf{z}_i\}$, plus a few noninformative rank-one spikes. In particular, these rank-one spikes, as pointed out by Remark 2.4 of [20], only depend on the kernel function, and do not contain any information about $\{\mathbf{x}_i\}_{1 \leq i \leq n}$; meanwhile, the empirical spectral distribution of \mathbf{K}_n will be governed by that of the noise Gram matrix and converges to the Marchenko-Pastur law [47]. In essence, there is a phase transition at $\alpha = \beta + 1$. See also Section 5 for more discussions.

Remark 3.4. There are fundamental advantages of the proposed bandwidth. Under the high-dimensional setup (1.2), most of the existing literature regarding the kernel random matrix \mathbf{K}_n focus on a pre-specified fixed bandwidth [18, 21, 22, 26]. In particular, when $\sigma = 1$, as they mainly deal with the null cases, $h_n = Cp$ is chosen for some constant $C > 0$, since the total noise is $\text{tr}(\text{Cov}(\mathbf{z}_i)) = p$. In contrast, under the non-null regime $\alpha > \beta + 1$ considered in the current study, if we still choose $h_n = Cp$, the bandwidth may be too small compared to the signal ($\asymp n^\alpha$) so that the decay of the kernel function forces each sample to be "blind" of the other nearby samples. Especially, as shown in Theorem 2.7 of [20], when the signals are strong enough so that $\alpha > \beta + 3$, if we still choose $h_n = Cp$, then we have $\lambda_i(\mathbf{K}_n) \rightarrow 1$ for all $1 \leq i \leq n$ with high probability. In this case, the kernel matrix converges to identity and becomes useless. In comparison, under our non-null regime $\alpha > \beta + 1$, our theory suggests one should choose $h_n \asymp rn^\alpha$. In this connection, although both r and α are generally unknown, our proposed bandwidth selection procedure is able to achieve this automatically from the data. In other words, as will be seen in the proof of Theorem 3.2, our proposed method is guaranteed to select $h_n \approx rn^\alpha$ with high probability.

3.3 Spectral Convergence to Population Integral Operator

So far we have shown that our proposed low-dimensional spectral embeddings converge to those associated to the noiseless random samples $\{\mathbf{x}_i\}_{1 \leq i \leq n}$. However, it is still unclear how these embeddings relate to the underlying manifold \mathcal{M} . Answering this question is important as to understand the proper interpretation of these embeddings.

Our next result concerns the limiting behavior of the eigenvalues and eigenvectors of \mathbf{K}_n , as characterized by a deterministic integral operator defined over the low-dimensional manifold. Before stating our main result, we first introduce a few notations from operator theory.

Recall that \mathbf{P} is the probability measure on \mathbb{R}^r for $\{\mathbf{x}_i^0\}_{i \in [n]}$ in (3.3) and \mathbf{OR} is the rotation matrix satisfying (3.1). Let

$$\mathcal{M}_0 = \{\mathbf{OR}\mathbf{x} : \mathbf{x} \in \mathcal{M} \subseteq \mathbb{R}^p\},$$

be the underlying manifold \mathcal{M} after rotation. We define $\tilde{\mathbf{P}}$ as the probability measure on \mathcal{M}_0 for $\{\mathbf{x}_i^0\}_{1 \leq i \leq n}$, which is also \mathbf{P} embedded into \mathbb{R}^p such that for $\mathbf{x} = (\mathbf{x}, 0, \dots, 0) \in \mathcal{M}$, we have $\tilde{\mathbf{P}}(\mathbf{x}) = \mathbf{P}(\mathbf{x})$. Accordingly, we define the population integral operator $\tilde{\mathcal{K}}$ such that for any $f \in \mathcal{L}_2(\mathbb{R}^p, \tilde{\mathbf{P}})$, we have

$$\tilde{\mathcal{K}}f(\mathbf{x}) = \int \exp\left(-\frac{\|\mathbf{x} - \mathbf{y}\|_2^2}{\mathbf{h}}\right) f(\mathbf{y}) \tilde{\mathbf{P}}(d\mathbf{y}), \quad \mathbf{x} \in \mathcal{M}_0, \quad (3.15)$$

where we recall that $\mathbf{h} = \sum_{i=1}^r \theta_i + p\sigma^2$.

Clearly, the eigenvalues and eigenfunctions of $\tilde{\mathcal{K}}$, denoted as $\{\tilde{\gamma}_i\}_{i \geq 1}$ and $\{\tilde{\phi}_i(\mathbf{x})\}_{i \geq 1}$ satisfy that

$$\tilde{\gamma}_i = \gamma_i, \quad \tilde{\phi}_i(\mathbf{x}) = \phi_i(\mathbf{x}), \quad \text{for } i \geq 1. \quad (3.16)$$

Moreover, let $\hat{\mathbf{P}}_n$ be the empirical distribution of the noisy samples $\{\mathbf{y}_i^0\}_{1 \leq i \leq n}$. Then the corresponding empirical operator $\hat{\mathcal{K}}_n$ is defined by

$$\hat{\mathcal{K}}_n f(\mathbf{x}) = \int \exp\left(-\frac{\|\mathbf{x} - \mathbf{y}\|_2^2}{h_n}\right) f(\mathbf{y}) \hat{\mathbf{P}}_n(d\mathbf{y}) = \frac{1}{n} \sum_{i=1}^n \exp\left(-\frac{\|\mathbf{x} - \mathbf{y}_i^0\|_2^2}{h_n}\right) f(\mathbf{y}_i^0), \quad \mathbf{x} \in \mathbb{R}^p. \quad (3.17)$$

It is easy to see that (for example, see the discussion of Section 2.2 of [58]), for $h_n \asymp h$, the eigenvalues of $\widehat{\mathcal{K}}_n$ coincide with $n^{-1}\mathbf{K}_n$, and for any eigenvalue $\lambda_i > 0$ of $\widehat{\mathcal{K}}_n$, the corresponding eigenfunction $\widehat{\phi}_i^{(n)}$ satisfies

$$\widehat{\phi}_i^{(n)}(\mathbf{x}) = \frac{1}{\lambda_i \sqrt{n}} \sum_{j=1}^n \exp\left(-\frac{\|\mathbf{x} - \mathbf{y}_j^0\|_2^2}{h_n}\right) u_{ij}, \quad \mathbf{x} \in \mathbb{R}^p, \quad (3.18)$$

and $\|\widehat{\phi}_i^{(n)}\|_{\widehat{\mathbf{P}}_n} = 1$, where u_{ij} is the j -th component of \mathbf{u}_i , the i -th eigenvector of \mathbf{K}_n . In particular, we have

$$\widehat{\phi}_i^{(n)}(\mathbf{y}_j^0) = \sqrt{n} u_{ij}, \quad \text{for all } j \in [n], \quad (3.19)$$

so that the eigenvector \mathbf{u}_i can be interpreted as the discretized i -th empirical eigenfunction $\widehat{\phi}_i^{(n)}$ evaluated at the noisy samples $\{\mathbf{y}_i^0\}_{1 \leq i \leq n}$. Finally, for some constant $\tau > 0$, we denote the integer $\mathbf{K} \equiv \mathbf{K}(\tau)$ as

$$\mathbf{K} \equiv \mathbf{K}(\tau) := \arg \max \{1 \leq i \leq n : \gamma_i \geq \tau\}. \quad (3.20)$$

In order to describe the convergence of eigenfunctions, we consider an RKHS \mathcal{H}_K for functions defined on $\text{supp}(\widehat{\mathbf{P}}) = \mathcal{M}_0$, associated with the kernel function $K(\cdot, \cdot) : \mathcal{M}_0 \times \mathcal{M}_0 \rightarrow \mathbb{R}$ such that

$$K(\mathbf{x}, \mathbf{y}) = \exp\left\{-\frac{\|\mathbf{x} - \mathbf{y}\|_2^2}{h}\right\}. \quad (3.21)$$

Specifically, we define \mathcal{H}_K as the completion of the linear span of the set of functions $\{K_{\mathbf{x}} = K(\mathbf{x}, \cdot) : \mathbf{x} \in \mathcal{M}_0\}$, with the inner product denoted as $\langle \cdot, \cdot \rangle_K$ satisfying $\langle K(\mathbf{x}, \cdot), K(\mathbf{y}, \cdot) \rangle_K = K(\mathbf{x}, \mathbf{y})$ and the reproducing property $\langle K(\mathbf{x}, \cdot), f \rangle_K = f(\mathbf{x})$ for any $f \in \mathcal{H}_K$ (see [8, 46] for systematic treatments of RKHS).

Theorem 3.5. *Under the assumptions of Theorem 3.2, the following results hold.*

1. (Eigenvalue convergence) *We have*

$$\max_{i \in [n]} |\lambda_i - \gamma_i| = \mathcal{O}_{\prec} \left(\frac{1}{\sqrt{n}} + \frac{1}{rn^{\alpha-\beta-1}} \right). \quad (3.22)$$

2. (Eigenfunction convergence) *For \mathbf{K} in (3.20) and $1 \leq i \leq \mathbf{K}$, if we restrict $\widehat{\phi}_i^{(n)}$ on \mathcal{M}_0 , then we have $\widehat{\phi}_i^{(n)} \in \mathcal{H}_K$ and*

$$\left\| \sqrt{\lambda_i} \widehat{\phi}_i^{(n)} - \sqrt{\gamma_i} \widetilde{\phi}_i \right\|_K = \mathcal{O}_{\prec} \left(\frac{1}{\sqrt{n}} + \frac{1}{rn^{\alpha-\beta-1}} + \left[\frac{1}{\sqrt{n}} + \frac{1}{rn^{\alpha-\beta-1}} \right]^{1/2} \frac{1}{r_i} \right), \quad (3.23)$$

where $\sqrt{\gamma_i} \widetilde{\phi}_i$ is the normalized eigenfunction of \mathcal{K} in \mathcal{H}_K satisfying $\|\sqrt{\gamma_i} \widetilde{\phi}_i\|_K = 1$, and $\|\cdot\|_K$ is the norm induced by the inner product $\langle \cdot, \cdot \rangle_K$.

Theorem 3.5 establishes the spectral convergence of the kernel matrix $n^{-1}\mathbf{K}_n$ to the population integral operator $\widetilde{\mathcal{K}}$ given by (3.15) in \mathcal{H}_K . On the one hand, (3.22) demonstrates that the deterministic limits of the eigenvalues $\{\lambda_i\}_{i \in [n]}$ are those of the integral operator $\widetilde{\mathcal{K}}$. On the other hand, (3.23) indicates that

the empirical eigenfunctions $\widehat{\phi}_i^{(n)}$, after proper rescaling, can also be regarded as an approximation of the population eigenfunctions $\widetilde{\phi}_i$ in an average manner. In particular, Theorem 3.5 implies that for any $1 \leq i \leq K$,

$$\lambda_i \mathbf{u}_i = \frac{\lambda_i}{\sqrt{n}} \cdot (\widetilde{\phi}_i^{(n)}(\mathbf{y}_1^0), \widetilde{\phi}_i^{(n)}(\mathbf{y}_2^0), \dots, \widetilde{\phi}_i^{(n)}(\mathbf{y}_n^0))^\top \approx \frac{\gamma_i}{\sqrt{n}} \cdot (\widetilde{\phi}_i(\mathbf{y}_1^0), \widetilde{\phi}_i(\mathbf{y}_2^0), \dots, \widetilde{\phi}_i(\mathbf{y}_n^0))^\top, \quad (3.24)$$

so that as long as $\Omega \subseteq \{1, 2, \dots, K\}$, the final low-dimensional embedding $\mathbf{U}_\Omega \Lambda_\Omega$ is approximately the leading K eigenfunctions evaluated at the rotated data $\{\mathbf{y}_i^0\}_{1 \leq i \leq n}$, and weighted by their corresponding eigenvalues $\{\gamma_i\}$. In other words, each coordinate of the final embedding is essentially a nonlinear transform of the original data, by some functions uniquely determined by the population integral operator $\widetilde{\mathcal{K}}$. This explains why our proposed method may capture important geometric features of the underlying manifold, and what kind of geometric features our method aims at.

As a comparison, existing methods such as Laplacian eigenmap, DM, or LLE, have their final embeddings correspond asymptotically to the Laplace-Beltrami differential operator evaluated at low-dimensional noiseless data. The fundamental distinction between integral and differential operators indicates the potential advantage of the proposed method over these existing methods, especially for high-dimensional noisy datasets as indicated by our real data analysis (Section 4.2). In this respect, Theorem 3.5 provides a systematic way to understand the general geometric interpretation of the proposed low-dimensional embedding, although their concrete meanings may vary from case to case. To better illustrate this, in Appendix C we consider a specific probability measure \mathbb{P} , obtain the explicit forms of its corresponding eigenvalues and eigenfunctions, and demonstrate their geometric interpretations accordingly.

4 Numerical Studies

We provide numerical simulations and three real data examples to illustrate the usefulness of our proposed method. Especially, in Section 4.1, we show that our adaptive bandwidth selection scheme (2.2) is robust and outperforms other existing methods. In Section 4.2, we compare our proposed embedding method (Algorithm 1) with various existing methods and show its outstanding performance.

4.1 Simulations

We conduct numerical experiments to evaluate the performance of the proposed bandwidth selection procedure (2.2) compared to some existing bandwidth methods in terms of the final embedding quality. To better demonstrate the wide range of applicability of the proposed method, we consider model (1.1) under three different settings of signal manifolds, and assess the quality of spectral embeddings as obtained from Steps 2 and 3 of Algorithm 1 under various bandwidths.

Specifically, we set $p = 300$ and $n = 300$, and generate $\mathbf{z}_i \sim_{i.i.d.} \mathcal{N}(\mathbf{0}, \mathbf{I}_p)$. For the signal samples $\{\mathbf{x}_i\}_{1 \leq i \leq n}$, we set $\mathbf{x}_i = (\mathbf{x}_i, 0, \dots, 0)$ for some $\mathbf{x}_i \in \mathbb{R}^r$, and generate $\{\mathbf{x}_i\}_{1 \leq i \leq n}$ from one of the following settings:

- Nested spheres manifold with $r = 6$: for some global scaling parameter $\theta > 0$, we set $\mathbf{x}_i = \theta \mathbf{x}'_i$ and generate *i.i.d.* samples $\{\mathbf{x}'_i\}_{1 \leq i \leq n}$ from a mixture model of nested spheres $\sum_{i=1}^6 w_i P_i$, where $\{P_i\}_{1 \leq i \leq 6}$ are uniform distributions on nested spheres in \mathbb{R}^6 of radii $\{1, 2, 3, 4, 5, 6\}$ respectively, and the cluster proportion vector $(w_1, w_2, \dots, w_6) = (0.1, 0.1, 0.1, 0.15, 0.25, 0.3)$.
- “Smiley face” manifold with $r = 2$: for some global scaling parameter $\theta > 0$, we set $\mathbf{x}_i = \theta \mathbf{x}'_i$ and generate *i.i.d.* samples $\{\mathbf{x}'_i\}_{1 \leq i \leq n}$ from a two-dimensional “smiley face” as shown in Figure 1 left.

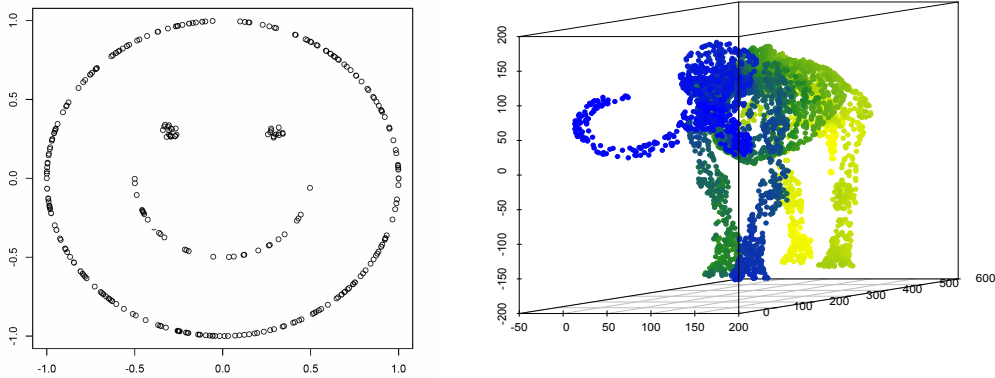


Figure 1: Left: the “smiley face” manifold. Right: the “mammoth” manifold, where the colors are made to better visualize the manifold in two dimension.

- “Mammoth” manifold with $r = 3$: for some global scaling parameter $\theta > 0$, we set $\mathbf{x}_i = \theta \mathbf{x}'_i$ and generate *i.i.d.* samples $\{\mathbf{x}'_i\}_{1 \leq i \leq n}$ from a three-dimensional “mammoth” as shown in Figure 1 right.

The global scaling parameter θ characterizes the overall signal-to-noise ratio, which plays the similar role as the term $n^{\alpha-\beta}$ in our theoretical results. In addition to the proposed adaptive bandwidth selection scheme, we also consider (i) the fixed bandwidth $h_n \equiv p$, which has been used in many existing works such as [18, 21, 22, 25, 26, 27], and (ii) the data-driven bandwidth selection method, denoted as “SBY,” proposed by [58]. We evaluate the above bandwidths by comparing the corresponding low-dimensional spectral embeddings $\mathbf{U}_\Omega \mathbf{\Lambda}_\Omega$ for $\Omega = \{1, 2, \dots, r\}$ of the high-dimensional noisy data $\{\mathbf{y}_i\}_{1 \leq i \leq n}$, and the actual low-dimensional noiseless samples $\{\mathbf{x}_i\}_{1 \leq i \leq n}$. To do that, we calculate the pairwise distance matrices $\mathbf{D}_{embed} \in \mathbb{R}^{n \times n}$ from the rows of $\mathbf{U}_\Omega \mathbf{\Lambda}_\Omega$, and $\mathbf{D}_x \in \mathbb{R}^{n \times n}$ from $\{\mathbf{x}_i\}_{1 \leq i \leq n}$, and characterize their concordance by the correlation measure

$$\text{Concordance} = \frac{\langle \mathbf{D}_{embed}, \mathbf{D}_x \rangle}{\|\mathbf{D}_{embed}\|_F \|\mathbf{D}_x\|_F}, \quad (4.1)$$

which is invariant to any scaling and rotations of the low-dimensional embeddings. Presumably, a good bandwidth selection should lead to higher concordance between the final embeddings and the original low-dimensional manifolds.

In Figure 2, we show the concordance evaluated for each bandwidth selection method over a variety of signal-to-noise ratios as quantified by θ , under each of the three manifold settings. In particular, to demonstrate the advantage and flexibility of the proposed method, we consider $\omega \in \{0.05, 0.25, 0.5, 0.75, 0.95\}$. From Figure 2, we observe that the proposed method has superior performance compared to $h = p$ and SBY in all the three manifolds, and across almost all the signal-to-noise ratios. The commonly used bandwidth $h = p$ only shows comparable performance in the “smiley face” example when signal-to-noise ratio is relatively low; the SBY method has poor performance throughout, probably as a result of ignorance of high-dimensionality of the noise. Importantly, the advantage of the proposed method is not sensitive to the values of ω , and can be more significant when the signal-to-noise ratio is larger. In Appendix D, we show

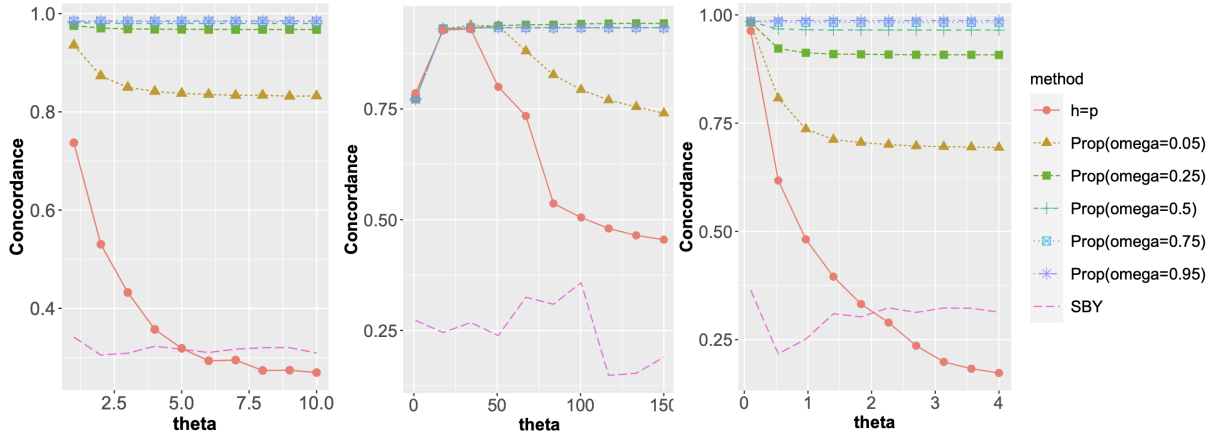


Figure 2: Comparison of bandwidth selection methods through the concordance in (4.1). Left: the nested sphere mixture manifold; Middle: the “smiley face” manifold; Right: the “mammoth” manifold. Here $h = p$ means that we apply Algorithm 1 with Step 1 replaced by using $h \equiv h_n = p$, SBY means that Step 1 is replaced by the bandwidth selection method of [58], $\text{Prop}(\omega = 0.05)$ means that we completely apply our proposed method Algorithm 1 where in Step 1 $\omega = 0.05$. Similar meanings apply for the other notations.

that ω selected by a data-driven resampling approach can achieve equally good performances in these examples. These numerical results indicate that accounting for the data high-dimensionality and noise impact is important for our kernel spectral embedding method to perform well, and our proposed bandwidth selection algorithm is reliable in that respect.

4.2 Applications to Real-World Datasets

To illustrate the proposed method and its numerical advantage over various existing methods in diverse applications, we analyze three real datasets with distinct underlying manifold structures.

4.2.1 Pseudotemporal Ordering of Single Cells

Our first example concerns pseudotemporal ordering of single cells. As an important problem in single-cell biology, pseudotemporal cell ordering aims to determine the pattern of a dynamic process experienced by cells and then arrange cells according to their progression through the process, based on single-cell RNA-Seq data collected at multiple time points. In the following, we show that our proposed embedding method is able to capture such an underlying progression path as a one-dimensional manifold, and therefore to help determine a more precise ordering of cells, compared to the existing state-of-art methods. The dataset consists of single-cell RNA sequencing reads for 149 human primordial germ cells ranging from 4 weeks to 19 weeks old [33]. Specifically, there are 6 cells of 4 weeks old, 37 cells of 7 weeks old, 20 cells of 10 weeks old, 27 cells of 11 weeks old, and 57 cells of 19 weeks old; these are treated as the ground truth for cell ordering. The raw count data were preprocessed, normalized, and scaled by following the standard procedure (R functions `CreateSeuratObject`, `NormalizeData` and `ScaleData` under default settings) as

incorporated in the R package `Seurat`¹. We also applied the R function `FindVariableFeatures` in `Seurat` to identify $p \in \{2500, 3000, 3500, 4000\}$ most variable genes for subsequent analysis. The final dataset consists of standardized expression levels of p genes for the 149 cells. We apply our proposed method with a variety of $\omega \in \{0.25, 0.5, 0.75\}$ and we consider a two-dimensional embedding $\Omega = \{1, 2\}$, where the one-dimensional manifold is already clearly captured; see left of Figure 3 for an illustration.

Observing that the path manifold is aligned with the second eigenvector, we order the cells according to their values in the second eigenvector. Inferred cell orders are also obtained using state-of-art cell ordering algorithms such as TSCAN [36], SCORPIUS [16], SerialRank [30], and the classical PCA. Note that SerialRank essentially has Laplacian eigenmap as its core. For TSCAN and SCORPIUS, we applied functions from their R packages² under the default settings. To evaluate the quality of the inferred orders, we compare them with the ground truth by evaluating their respective Kendall’s tau statistic.

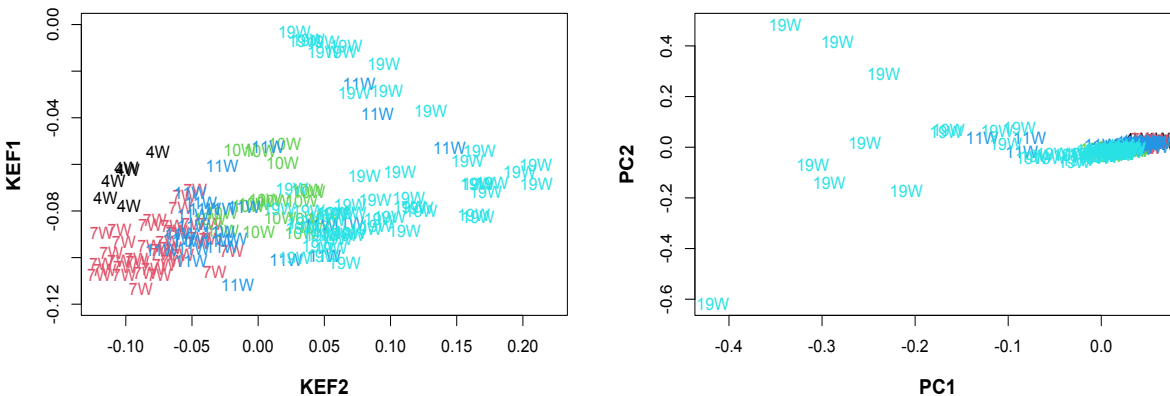


Figure 3: Comparison between principal component embeddings (PCs) and proposed kernel embeddings (KEFs) when $p = 3000$, where the cells were labelled and colored according to their actual time courses.

On the left of Figure 4, the temporal ordering based on the proposed method ($\omega = 0.5$) aligns better with the actual cell order than the other methods, with almost three-fold improvement over the second best method TSCAN in Kendall’s tau on average. The superiority of the proposed method is not sensitive to the dimension p , or the quantile parameter ω . See Appendix D for similar results with $\omega = 0.25$ and 0.75 .

Finally, in Figure 3 we show the scatter plots of the 2-dimensional embeddings based on PCA and the proposed method, denoted as KEF standing for kernel eigenfunctions, when $p = 3000$. The advantage of the proposed embedding over its linear counterpart, such as informativeness and robustness to outliers, is visible and significant.

4.2.2 Cell Cycle Reconstruction

Our second example concerns reconstruction of the cell cycle from single-cell RNA-Seq data. The cell cycle, or cell-division cycle, is the series of events that take place in a cell that cause it to divide into two daughter

¹<https://cran.r-project.org/web/packages/Seurat/index.html>

²<https://github.com/zji90/TSCAN>, and <https://cran.rstudio.com/web/packages/SCORPIUS/index.html>

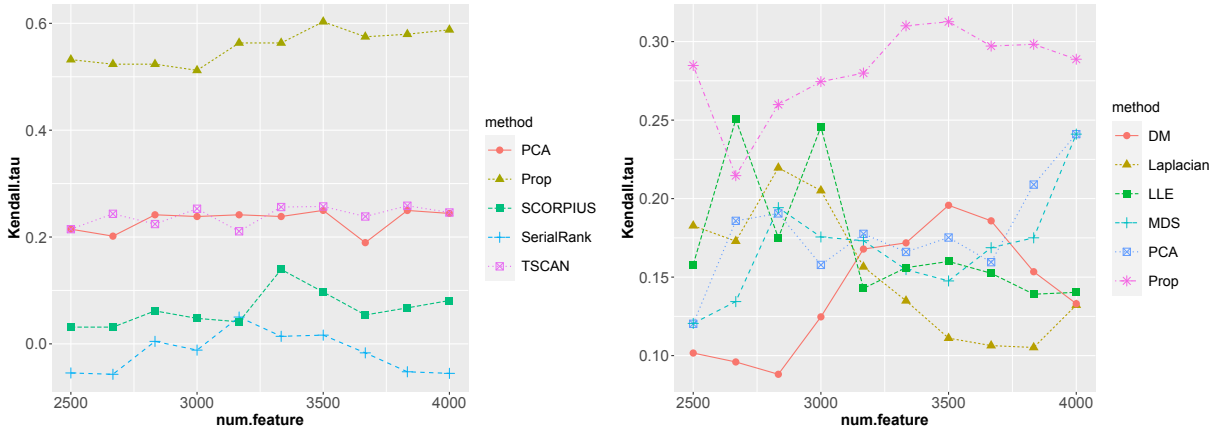


Figure 4: Left: comparison of five methods for cell ordering in Section 4.2.1. Right: comparison of six methods for cell cycle reconstruction in Section 4.2.2. In both plots, the proposed method Algorithm 1 uses $\omega = 0.5$. Similar results with $\omega = 0.25$ and 0.75 can be found in Appendix D.

cells³. Determining the cell cycle stages of individual cells analyzed during development is important for understanding its wide-ranging effects on cellular physiology and gene expression profiles. Our second dataset contains 288 mouse embryonic stem cells, whose cell cycle stages were determined using flow cytometry sorting. As a result, one-third (96) of the cells are in the G1 stage, one-third in the S stage, and the rest in the G2M stage. The raw count data were preprocessed and normalized using the same method as in Section 4.2.1, leading to a dataset consisting of standardized expression levels of $p \in \{2500, 3000, 3500, 4000\}$ most variable genes for the 288 cells. Again, we apply our proposed method with a variety of $\omega \in \{0.25, 0.5, 0.75\}$. Observing that the leading eigenvector is approximately a constant vector and therefore non-informative, we consider a two-dimensional embedding with $\Omega = \{2, 3\}$, expected to capture the underlying circle manifold. As a comparison, we also obtain two-dimensional embeddings based on PCA, MDS, Laplacian eigenmap, LLE and DM, using functions implemented in the R package `dimRed` under their default settings. To recover the cell cycle stages, or the underlying position of the cells on the circle manifold, we project each embedding to the two-dimensional unit circle, and then identify the cell stages with their respective angles on the unit circle. We compare the reconstruction performance of different methods based on their Kendall's tau distance to the true stages, up to a possible circular shift of the reconstructed cycles.

The right panel of Figure 4 shows that our proposed method has outstanding performance compared to the other methods. In addition, Figure 5 shows the unit-circle projections of the two-dimensional embeddings obtained from each method under $p = 3000$. It can be seen that the cells are most separated and well-ordered according to their true cycle stages along the unit-circle reconstructed by the proposed method, demonstrating its superiority over the other methods.

³https://en.wikipedia.org/wiki/Cell_cycle

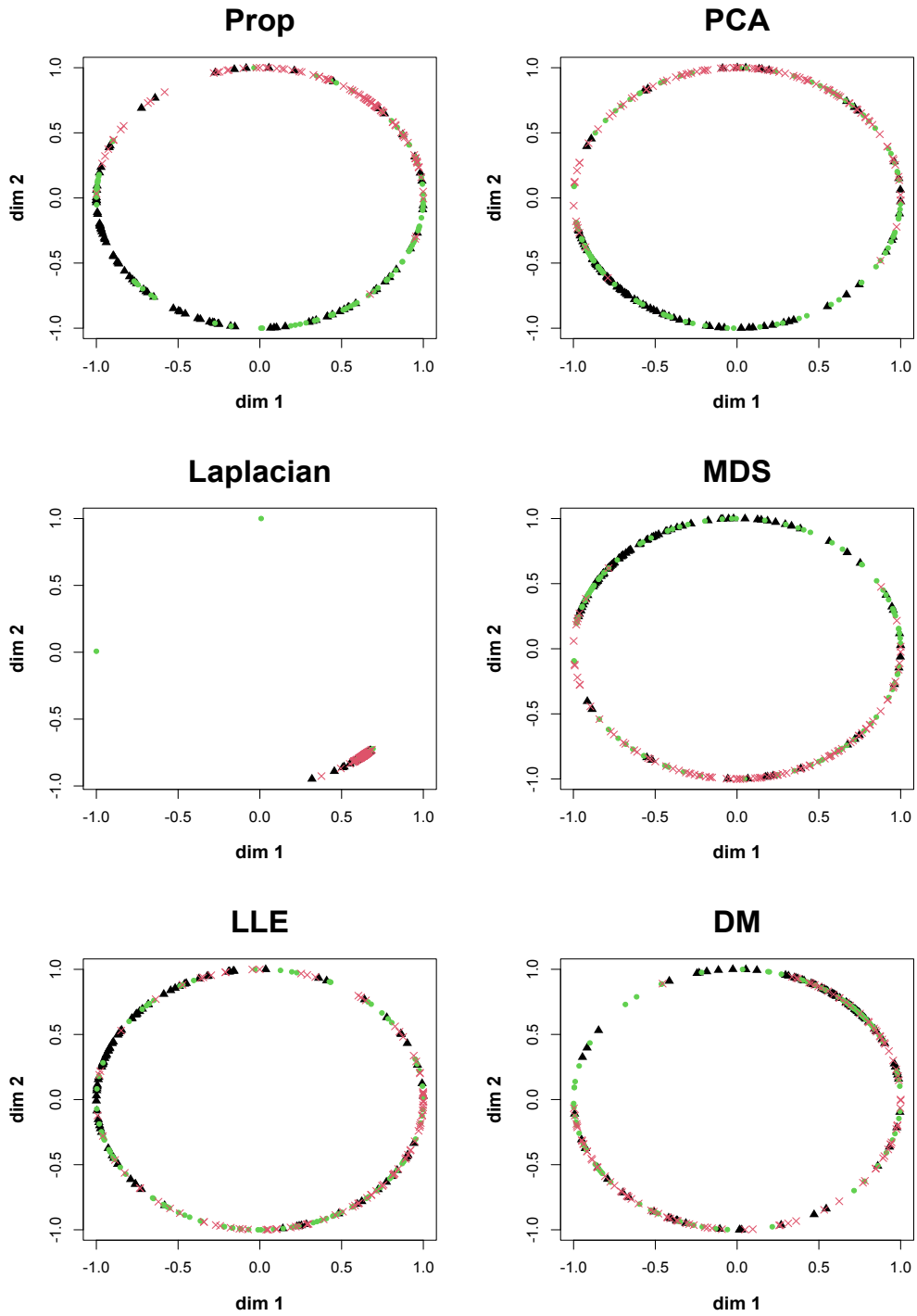


Figure 5: Comparison of reconstructed cell cycles based on six embedding methods when $p = 3000$. Red crosses: cells in G1 stage. Green dots: cells in S stage. Black triangles: cells in G2M stage.

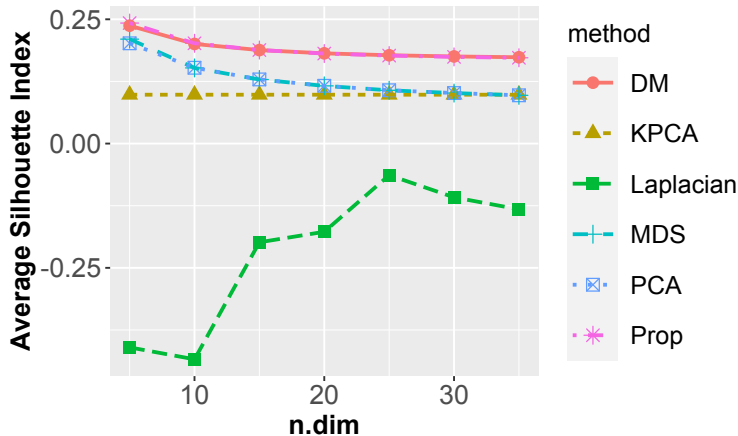


Figure 6: Comparison of six embedding methods for $n = 3946$ samples from the MNIST data. The Silhouette index indicates how much of the underlying cluster pattern is preserved in the low-dimensional embeddings.

4.2.3 Clustering of Hand-Written Digits

Our last example concerns the MNIST⁴ dataset containing images of hand-written digits. Specifically, we focus on $n = 3946$ images of hand-written digits “2,” “4,” “6” and “8,” among which there are about 1000 images for each digit. As each image contains 28×28 pixels, they can be treated as 784-dimensional vectors. We apply six different low-dimensional embedding methods, namely DM, kPCA as defined in Section 2.2, Laplacian eigenmap, MDS, PCA and the proposed method, for a variety of embedding dimensions $n.\text{dim} \in \{5, 10, 15, 20, 25, 30, 35\}$. In particular, to ensure fairness in comparison, we have not included two-stage algorithms such as tSNE and UMAP, which essentially take one of the above kernel spectral embeddings as an initialization, and then refine the low-dimensional embedding to make the cluster pattern more salient based on some local-metric adjustment [48, 4, 45, 14].

We evaluate the embedding quality of a method by calculating the average Silhouette index [52] of the final low-dimensional embedding with respect to the underlying true cluster membership. In general, a higher average Silhouette index of a method indicates the underlying clusters are more separate in the final embedding. Again, for the proposed method we use $\omega = 0.5$. Similar results are obtained for $\omega \in \{0.25, 0.75\}$ as in Appendix D. In Figure 6, we found that our proposed method along with DM has overall the best performance among the six methods. In particular, although the standard kPCA differs from our proposed method only by an additional mean shift (2.5), in all cases its embedding quality is clearly worse than the latter, demonstrating the important distinction between kPCA and the proposed method, and the potential advantage of the latter in applications.

5 Discussion

We propose a kernel-spectral embedding algorithm for learning low-dimensional nonlinear structure from high-dimensional noisy datasets under a manifold setup. A key component is to develop an adaptive band-

⁴<http://yann.lecun.com/exdb/mnist/>

width selection procedure that is free from prior knowledge of the manifold. Our proposed method is theoretically justified and our embeddings correspond to an integral operator from the RKHS associated to the underlying manifold. While our results pave the way towards statistical foundations for nonlinear dimension reduction, manifold learning, among others, there are various problems to be investigated further. We now highlight a few of them.

First, in this paper, we focus on the prototypical Gaussian kernel for the construction of the low-dimensional embeddings. However, this is only an initial step towards interpretable manifold learning under high-dimensional noisy data, and our results stand as a vintage point for exploring and understanding similar kernel-spectral embedding algorithms based on other kernel functions, such as cosine kernel, polynomial kernel, inner-product kernel, self-tune kernel, etc.

Second, in Part 2 of Theorem 3.5, the convergence of eigenfunctions is obtained under the kernel-induced norm in \mathcal{H}_K , characterizing the closeness in a global manner. In some applications, a more precise local characterization of the final embedding is needed. For example, one needs to study the convergence property of the eigenfunctions under the L_∞ norm, defined by $\|f\|_\infty = \sup_{\mathbf{x}} |f(\mathbf{x})|$. However, to our best knowledge, even in the noiseless setting, the L_∞ convergence has only been studied to some extent for normalized integral operator in [71, 70] and the linear differential Laplace–Beltrami operator in [15, 24, 74]. Less is known for the unnormalized integral operator as used in the current paper. Moreover, to understand the convergence in L_∞ norm for the noisy datasets, in contrast to (3.14), we also need to study the ℓ_∞ convergence of the eigenvectors of the kernel random matrices. The analysis requires a more sophisticated argument from random matrix theory as in [5, 28]. We will pursue these directions in future works.

Additionally, the current work mainly concerns the super-critical non-null regime $\alpha > \beta + 1$. When $\alpha = \beta + 1$, according to (2) of Theorem 3.1 of [20], since the signal part has a comparable strength as the noise part, neither of them dominates the other in terms of the behavior of $n^{-1}\mathbf{K}_n$. Similar results have also been established in [25]. In this critical regime, to better utilize the kernel matrix $n^{-1}\mathbf{K}_n$, one needs to develop a high-dimensional nonlinear signal and noise separation procedure. However, a detailed account for this problem is beyond the scope of this paper.

Finally, in the current paper, we use an integral operator to learn the geometric structure of the underlying manifold. To enhance our understanding of the nonlinear structures, it is of interest to explore the relationship between the eigenfunctions of our integral operator and those of the Laplace–Beltrami operator. The main challenge is that, in the high-dimensional noisy setting, the normalized graph Laplacian would no longer converge to the Laplace–Beltrami operator [20], so that novel methodologies are needed to facilitate the comparison. Moreover, in the current paper, we focus on an RKHS-based method. It will be interesting to study the graph based methods for high-dimensional noisy datasets under the setting (1.1) and (1.2).

A Preliminary Results

In this section, we summarize and prove some useful technical results, which play an important role in our proof of the main results.

A.1 Spectral convergence of integral operators in RKHS

We summarize and prove the spectral convergence of the empirical integral operator to the population integral operator. Most of the results can be found in [13, 42, 51, 57, 58, 63, 64]. Consider that we observe n i.i.d. samples $\{\mathbf{x}_i\}_{1 \leq i \leq n}$ drawn from some probability distribution \mathbb{P} in \mathbb{R}^p . Then the population integral

operator \mathcal{K} with respect to \mathbf{P} is defined by

$$\mathcal{K}f(\mathbf{x}) = \int \exp\left(-\frac{\|\mathbf{x} - \mathbf{y}\|_2^2}{h}\right) f(\mathbf{y}) \mathbf{P}(d\mathbf{y}), \quad \mathbf{x}, \mathbf{y} \in \text{supp}(\mathbf{P}), \quad (\text{A.1})$$

and its empirical counterpart \mathcal{K}_n defined by

$$\mathcal{K}_n f(\mathbf{x}) = \int \exp\left(-\frac{\|\mathbf{x} - \mathbf{y}\|_2^2}{h}\right) f(\mathbf{y}) \mathbf{P}_n(d\mathbf{y}) = \frac{1}{n} \sum_{i=1}^n \exp\left(-\frac{\|\mathbf{x} - \mathbf{x}_i\|_2^2}{h}\right) f(\mathbf{x}_i), \quad \mathbf{x} \in \text{supp}(\mathbf{P}). \quad (\text{A.2})$$

The Reproducing Kernel Hilbert Space (RKHS) \mathcal{H}_K associated with the kernel function

$$K(\mathbf{x}, \mathbf{y}) = \exp\left\{-\frac{\|\mathbf{x} - \mathbf{y}\|_2^2}{h}\right\}, \quad \mathbf{x}, \mathbf{y} \in \text{supp}(\mathbf{P}), \quad (\text{A.3})$$

in (A.1) and (A.2) is defined as the completion of the linear span of the set of functions $\{K_{\mathbf{x}} = K(\mathbf{x}, \cdot) : \mathbf{x} \in \text{supp}(\mathbf{P})\}$ with the inner product denoted as $\langle \cdot, \cdot \rangle_K$ satisfying $\langle K(\mathbf{x}, \cdot), K(\mathbf{y}, \cdot) \rangle_K = K(\mathbf{x}, \mathbf{y})$ and the reproducing property $\langle K(\mathbf{x}, \cdot), f \rangle_K = f(\mathbf{x})$ for any $f \in \mathcal{H}_K$. Note that \mathcal{K} and \mathcal{K}_n may be considered as self-adjoint operators on \mathcal{H}_K , or on their respective L_2 spaces (that is, $\mathcal{L}_2(\Omega, \mathbf{P})$ and $\mathcal{L}_2(\Omega, \mathbf{P}_n)$, $\Omega = \text{supp}(\mathbf{P})$).

In addition, it is easy to see that (for example, see the discussion of Section 2.2 of [58]) the eigenvalues of \mathcal{K}_n coincide with $n^{-1}\mathbf{K}_n^*$, where $\mathbf{K}_n^* = (K(\mathbf{x}_i, \mathbf{x}_j))_{1 \leq i, j \leq n}$ with $K(\cdot, \cdot)$ given by (A.3). The eigenfunctions $\{\phi_i^{(n)}\}$ associated with nonzero eigenvalues $\{\mu_i\}$ of \mathcal{K}_n or $n^{-1}\mathbf{K}_n^*$ satisfy

$$\phi_i^{(n)}(\mathbf{x}) = \frac{1}{\mu_i \sqrt{n}} \sum_{j=1}^n \exp\left(-\frac{\|\mathbf{x} - \mathbf{x}_j\|_2^2}{h}\right) v_{ij}, \quad \mathbf{x} \in \text{supp}(\mathbf{P}), \quad (\text{A.4})$$

where $\mathbf{v}_i = (v_{i1}, v_{i2}, \dots, v_{in})^\top$ is the i -th eigenvector of $n^{-1}\mathbf{K}_n^*$, and that $\|\phi_i^{(n)}\|_{\mathbf{P}_n} = 1$.

In the following we will mainly consider them to be operators in \mathcal{H}_K to facilitate quantitative comparison. The following lemma concerns the convergence of the eigenvalues and eigenfunctions of \mathcal{K}_n to those of \mathcal{K} .

Lemma A.1. *For self-adjoint operators \mathcal{K} and \mathcal{K}_n on \mathcal{H}_K , defined by (A.1) and (A.2), we have*

$$\|\mathcal{K} - \mathcal{K}_n\| \prec \frac{1}{\sqrt{n}}. \quad (\text{A.5})$$

Let $\{\gamma_i\}$ and $\{\phi_i\}$ be the eigenvalues and eigenfunctions of \mathcal{K} . We define the i -th population eigen-gap as $r_i = \min\{\gamma_{i-1} - \gamma_i, \gamma_i - \gamma_{i+1}\}$. If $r_i \geq Cn^{-1/2+\epsilon}$ for some constant $C > 0$ and small $\epsilon > 0$, then the eigenfunctions $\{\phi_i^{(n)}\}$ of \mathcal{K}_n associated with nonzero eigenvalues satisfy

$$\left\| \sqrt{\gamma_i} \phi_i - \sqrt{\mu_i} \phi_i^{(n)} \right\|_K \prec \frac{1}{r_i \sqrt{n}}, \quad (\text{A.6})$$

where $\|\sqrt{\gamma_i} \phi_i\|_K = \|\sqrt{\mu_i} \phi_i^{(n)}\|_K = 1$, and $\|\phi_i^{(n)}\|_{\mathbf{P}_n} = 1$.

Proof. To obtain (A.5), according to [64, Proposition 1] or [51, Theorem 7], in view of our notion of stochastic domination, we have that

$$\|\mathcal{K} - \mathcal{K}_n\|_{\text{HS}} \prec \frac{1}{\sqrt{n}},$$

where we used the fact that the kernel function

$$K(\mathbf{x}, \mathbf{y}) = \exp \left\{ -\frac{\|\mathbf{x} - \mathbf{y}\|_2^2}{h} \right\},$$

in (A.1) and (A.2) is bounded. Then the result follows from the elementary relation $\|\mathcal{K} - \mathcal{K}_n\| \leq \|\mathcal{K} - \mathcal{K}_n\|_{\text{HS}}$.

For the eigenfunctions, the proof is similar to [64, Corollary 1] or [51, Theorem 12] using the perturbation argument as recorded in Lemma A.7. Specifically, from [64, Corollary 1], we have

$$\|\sqrt{\gamma_i} \phi_i - \Phi_i\|_K \prec \frac{1}{r_i \sqrt{n}}, \quad (\text{A.7})$$

where

$$\Phi_i(\mathbf{x}) = \frac{1}{\sqrt{n\mu_i}} \sum_{j=1}^n \exp \left(-\frac{\|\mathbf{x} - \mathbf{x}_j\|_2^2}{h} \right) v_{ij},$$

$\mathbf{v}_i = (v_{i1}, \dots, v_{in})^\top$ and μ_i are i -th eigenvector and eigenvalue of $\frac{1}{n} \mathbf{K}_n^* = n^{-1} (K(\mathbf{x}_i, \mathbf{x}_j))_{1 \leq i, j \leq n}$, respectively. By definition, we have

$$\phi_i^{(n)} = \frac{1}{\sqrt{n\mu_i}} \sum_{j=1}^n K(\mathbf{x}_i, \cdot) v_{ij} = \frac{1}{\sqrt{\mu_i}} \Phi_i,$$

this implies (A.6). Finally, direct calculation yields

$$\begin{aligned} \|\sqrt{\gamma_i} \phi_i\|_K^2 &= \gamma_i \langle \phi_i, \phi_i \rangle_K = \langle \mathcal{K} \phi_i, \phi_i \rangle_K = \left\langle \int K(\cdot, \mathbf{y}) \phi_i(\mathbf{y}) \mathbf{P}(\mathrm{d}\mathbf{y}), \phi_i \right\rangle_K \\ &= \int \langle K(\cdot, \mathbf{y}), \phi_i \rangle_K \phi_i(\mathbf{y}) \mathbf{P}(\mathrm{d}\mathbf{y}) = \int [\phi_i(\mathbf{y})]^2 \mathbf{P}(\mathrm{d}\mathbf{y}) = \|\phi_i\|_{\mathbf{P}}^2 = 1, \end{aligned}$$

and

$$\begin{aligned} \|\Phi_i\|_K^2 &= \left\langle \frac{1}{\sqrt{n\mu_i}} \sum_{j=1}^n K(\mathbf{x}_i, \cdot) v_{ij}, \frac{1}{\sqrt{n\mu_i}} \sum_{j=1}^n K(\mathbf{x}_i, \cdot) v_{ij} \right\rangle_K \\ &= \frac{1}{n\mu_i} \sum_{j=1}^n \sum_{k=1}^n v_{ij} v_{ik} \langle K(\mathbf{x}_j, \cdot), K(\mathbf{x}_k, \cdot) \rangle_K \\ &= \frac{1}{n\mu_i} \sum_{j=1}^n \sum_{k=1}^n v_{ij} v_{ik} K(\mathbf{x}_j, \mathbf{x}_k) \\ &= \frac{1}{\mu_i} \mathbf{v}_i^\top (n^{-1} \mathbf{K}_n^*) \mathbf{v}_i \\ &= 1, \end{aligned}$$

and

$$\begin{aligned}
\|\phi_i^{(n)}\|_{\mathbb{P}_n}^2 &= \left\langle \frac{1}{\sqrt{n\mu_i}} \sum_{j=1}^n K(\mathbf{x}_j, \cdot) v_{ij}, \frac{1}{\sqrt{n\mu_i}} \sum_{j=1}^n K(\mathbf{x}_j, \cdot) v_{ij} \right\rangle \\
&= \frac{1}{n\mu_i^2} \sum_{j=1}^n \sum_{k=1}^n v_{ij} v_{ik} \int K(\mathbf{x}_j, \mathbf{y}) K(\mathbf{x}_k, \mathbf{y}) \mathbb{P}_n(d\mathbf{y}) \\
&= \frac{1}{n^2 \mu_i^2} \sum_{j=1}^n \sum_{l=1}^n \sum_{k=1}^n v_{ij} v_{ik} K(\mathbf{x}_j, \mathbf{x}_l) K(\mathbf{x}_l, \mathbf{x}_k) \\
&= \frac{1}{\mu_i^2} \mathbf{v}_i^\top (n^{-1} \mathbf{K}_n^*)^2 \mathbf{v}_i \\
&= 1.
\end{aligned}$$

□

A.2 Concentration inequalities

Many of these results can be found or generalized from [20, 21]. We will consistently use stochastic domination to characterize the high-dimensional concentration. The first lemma collects some useful concentration inequalities.

Lemma A.2. *Suppose Assumption 3.1 holds. Then we have that*

$$\max_{i \neq j} \frac{1}{\sigma^2 p} |\mathbf{z}_i^\top \mathbf{z}_j| \prec n^{-1/2},$$

and

$$\max_i \left| \frac{1}{\sigma^2 p} \|\mathbf{z}_i\|_2^2 - 1 \right| \prec n^{-1/2}.$$

Proof. See Lemma A.4 of [20] or Lemmas A.1 and A.2 of [21].

□

The second lemma provides a sharp upper bound for the norm of \mathbf{K}_n^* .

Lemma A.3. *Suppose Assumption 3.1 holds. Let*

$$\mathbf{K}_n^* = (K^*(i, j))_{1 \leq i, j \leq n}, \quad K^*(i, j) = \exp\left(-\frac{\|\mathbf{x}_i - \mathbf{x}_j\|_2^2}{h}\right),$$

and

$$h = \sum_{i=1}^r \theta_i + p\sigma^2. \tag{A.8}$$

Then we have that

$$\|\mathbf{K}_n^*\| \prec n.$$

Proof. Note that $\max_{i, j} |K_n^*(i, j)| \prec 1$. The proof follows from Lemma A.6.

□

The third lemma collects the results on the concentration for the bandwidth selected according to Step 1 of the proposed Algorithm 1.

Lemma A.4. *Suppose Assumption 3.1 holds, $\alpha > \beta + 1$ and h_n is selected according to Algorithm 1. Then we have that*

$$\sum_{i=1}^r \theta_i + p\sigma^2 \prec h_n \prec \sum_{i=1}^r \theta_i + p\sigma^2.$$

Proof. Following the lines of the proof of equation (C.2) of [20], it is easy to see that with high probability, for some constants $C_1, C_2 > 0$

$$C_1 \left(\frac{1}{\log n} \sum_{i=1}^r \theta_i + p\sigma^2 \right) \leq h_n \leq C_2 \left(\log^2 n \sum_{i=1}^r \theta_i + p\sigma^2 \right).$$

Then the proof follows from the Assumption 3.1, $\alpha > \beta + 1$ and the notation of stochastic domination as in Definition 1.1. \square

A.3 Useful tools from linear algebra

Lemma A.5. *Suppose M is a real symmetric matrix with nonnegative entries and E is a real symmetric matrix. Then we have that*

$$s_1(M \circ E) \leq s_1(M) \max_{i,j} |E(i,j)|,$$

where $s_1(\cdot)$ is the largest singular value of the given matrix.

Proof. See Lemma A.5 of [26]. \square

Lemma A.6. *Let $A = (a_{ij})$ be a real $n \times n$ matrix. For $1 \leq i \leq n$, let $R_i = \sum_{j \neq i} |a_{ij}|$ be the sum of the absolute values of the non-diagonal entries in the i th row. Let $D(a_{ii}, R_i) \subset \mathbb{R}$ be a closed disc with center a_{ii} and radius R_i referred to as the Gershgorin disc. Then every eigenvalue of $A = (a_{ij})$ lies within at least one of the Gershgorin discs $D(a_{ii}, R_i)$, where $R_i = \sum_{j \neq i} |a_{ij}|$.*

Proof. See Section 6.1 of [35]. \square

Lemma A.7. *Let A and \widehat{A} be two compact positive self-adjoint operators on a Hilbert space \mathcal{H} , with non-decreasing eigenvalues $\{\lambda_j(A)\}$ and $\{\lambda_j(\widehat{A})\}$. Let w_k be a normalized eigenvector of A associated with the eigenvalue λ_k . If $l_k > 0$ satisfies*

$$\lambda_{k-1} - \lambda_k \geq l_k, \quad \lambda_k - \lambda_{k+1} \geq l_k, \quad \|A - \widehat{A}\| \leq \frac{l_k}{2},$$

then we have that

$$\|w_k - \widehat{w}_k\| \leq \frac{4}{l_k} \|A - \widehat{A}\|.$$

Proof. See Proposition 2 of [64]. \square

B Proof of Main Theoretical Results

We prove the main results, Theorems 3.2 and 3.5, in this section.

B.1 Proof of Theorem 3.2

In the following, according to the arguments of Section 3.1, without loss of generality, we will consider the reduced data $\{\mathbf{y}_i^0\}_{1 \leq i \leq n}$ and their related quantities $\{\mathbf{x}_i^0\}_{1 \leq i \leq n}$ and $\{\mathbf{z}_i^0\}_{1 \leq i \leq n}$. For simplicity, with a little bit abuse of notations, we omit their superscripts and denote them as $\{\mathbf{y}_i\}$, $\{\mathbf{x}_i\}$ and $\{\mathbf{z}_i\}$.

Eigenvalue convergence. It suffices to prove the result under the fixed bandwidth as in (A.8). The results under the bandwidth h_n as selected by Algorithm 1 follows from the same argument in view of Lemma A.4.

Under the bandwidth choice (A.8), with a slight abuse of notations, we can define the kernel matrices for $\mathbf{y}_i, \mathbf{x}_i$, and \mathbf{z}_i , as $\mathbf{K}_y, \mathbf{K}_x$ and \mathbf{K}_z , respectively. For example, $\mathbf{K}_x = (K(\mathbf{x}_i, \mathbf{x}_j))_{1 \leq i, j \leq n}$, where $K(\mathbf{x}_i, \mathbf{x}_j) = \exp(-\|\mathbf{x}_i - \mathbf{x}_j\|_2^2/h)$. Furthermore, we denote an auxiliary matrix \mathbf{K}_c whose (i, j) -th entry is given by

$$\mathbf{K}_c(i, j) = \exp\left(-\frac{2(\mathbf{x}_i - \mathbf{x}_j)^\top (\mathbf{z}_i - \mathbf{z}_j)}{h}\right), \quad (\text{B.1})$$

and define

$$\mathbf{E}_0 = \exp\left(-\frac{2\sigma^2 p}{h}\right) \mathbf{1}\mathbf{1}^\top + \left(1 - \exp\left(-\frac{2\sigma^2 p}{h}\right)\right) \mathbf{I}_n,$$

where $\mathbf{1} \in \mathbb{R}^n$ is a vector with all entries being unity. Let $\mathbf{A} \circ \mathbf{B}$ be the Hadamard product of two matrices \mathbf{A} and \mathbf{B} . We define another auxiliary matrix

$$\mathbf{K}_s = \mathbf{E}_0 \circ \mathbf{K}_x. \quad (\text{B.2})$$

Using the above notations and the trivial relation that

$$\mathbf{K}_s = (\mathbf{1}\mathbf{1}^\top) \circ \mathbf{K}_s, \quad \mathbf{K}_y = \mathbf{K}_x \circ \mathbf{K}_c \circ \mathbf{K}_z,$$

we readily see that

$$\begin{aligned} \mathbf{K}_y - \mathbf{K}_s &= [(\mathbf{K}_c - \mathbf{1}\mathbf{1}^\top) \circ \mathbf{K}_z \circ \mathbf{K}_x] + [(\mathbf{K}_z - \mathbf{E}_0) \circ \mathbf{K}_x] \\ &:= \mathcal{E}_1 + \mathcal{E}_2. \end{aligned} \quad (\text{B.3})$$

We first control \mathcal{E}_2 . Note that $\mathbf{K}_z(i, i) - \mathbf{E}_0(i, i) = 0$ for all $1 \leq i \leq n$. For $i \neq j$, set

$$\Delta(i, j) = \frac{\|\mathbf{z}_i - \mathbf{z}_j\|_2^2}{\sigma^2 p} - 2.$$

By the mean value theorem, we obtain that, for $i \neq j$,

$$\mathbf{K}_z(i, j) = \exp\left(-\frac{2\sigma^2 p}{h}\right) - \frac{\sigma^2 p}{h} \exp\left(-\frac{\zeta(i, j)\sigma^2 p}{h}\right) \Delta(i, j),$$

for some $\zeta(i, j)$ between $\frac{\|\mathbf{z}_i - \mathbf{z}_j\|_2^2}{\sigma^2 p}$ and 2. By Lemma A.2 and the assumption (1.2), we conclude that

$$\max_{i \neq j} |\Delta(i, j)| \prec \frac{1}{\sqrt{n}}, \quad \max_{i \neq j} \zeta(i, j) = 2 + \text{O}_\prec\left(\frac{1}{\sqrt{n}}\right).$$

Consequently, we have that

$$\max_{i, j} |\mathbf{K}_z(i, j) - \mathbf{E}_0(i, j)| \prec \frac{1}{\sqrt{n}}, \quad (\text{B.4})$$

as $\sigma^2 p/h \leq 1$. Since \mathbf{K}_x is symmetric with nonnegative entries, by (B.4) and Lemma A.5, we obtain that

$$\|\mathcal{E}_2\| \prec \frac{1}{\sqrt{n}} \|\mathbf{K}_x\|.$$

According to Lemma A.3, we have that

$$\|\mathbf{K}_x\| \prec n. \quad (\text{B.5})$$

This yields that

$$\frac{1}{n} \|\mathcal{E}_2\| \prec \frac{1}{\sqrt{n}}. \quad (\text{B.6})$$

Analogously, for \mathcal{E}_1 , applying Lemma A.5, we see that

$$\|\mathcal{E}_1\| \leq \left(\max_{i,j} |\mathbf{K}_c(i,j) - 1| \right) \cdot \max_{i,j} \mathbf{K}_z(i,j) \cdot \|\mathbf{K}_x\|.$$

On one hand, by (B.4) and the fact $\mathbf{K}_z(i,i) = 1$, we have that

$$\max_{i,j} \mathbf{K}_z(i,j) \prec 1.$$

Moreover, under Assumption 3.1, by (B.1), it is easy to see that

$$\max_{i,j} |\mathbf{K}_c(i,j) - 1| \leq \frac{2|(\mathbf{x}_i - \mathbf{x}_j)^\top (\mathbf{z}_i - \mathbf{z}_j)|}{h} \prec \frac{\sigma \sqrt{\sum_{i=1}^r \theta_i}}{\sigma^2 p + \sum_{i=1}^r \theta_i} \prec \sigma r^{-1/2} n^{-\alpha/2} \asymp r^{-1/2} n^{-\frac{\alpha-\beta}{2}}.$$

Together with (B.5), we immediately see that

$$\frac{1}{n} \|\mathcal{E}_1\| \prec r^{-1/2} n^{-\frac{\alpha-\beta}{2}}. \quad (\text{B.7})$$

Combining (B.6) and (B.7), we have that

$$\frac{1}{n} \|\mathbf{K}_y - \mathbf{K}_s\| \prec \frac{1}{\sqrt{n}} + r^{-1/2} n^{-\frac{\alpha-\beta}{2}} \prec \frac{1}{\sqrt{n}},$$

as $\alpha > \beta + 1$. Additionally, since $\mathbf{K}_x = (\mathbf{1}\mathbf{1}^\top) \circ \mathbf{K}_x$, using (B.2) and Lemma A.5, we have that for some constant $C > 0$, when n is large enough,

$$\frac{1}{n} \|\mathbf{K}_x - \mathbf{K}_s\| \leq \frac{1}{n} \|\mathbf{K}_x\| \cdot \max_{i,j} |\mathbf{E}_0(i,j) - 1| \prec \frac{\sigma^2 p}{h} \leq \frac{\sigma^2}{\sigma^2 + rn^{\alpha-1}} \prec Cr^{-1} n^{-(\alpha-\beta-1)},$$

where in the second step we used (B.5). This yields that

$$\frac{1}{n} \|\mathbf{K}_x - \mathbf{K}_y\| \prec \frac{1}{\sqrt{n}} + \frac{1}{rn^{\alpha-\beta-1}}. \quad (\text{B.8})$$

This completes our proof of the first part. \square

Eigenvector convergence. Then we prove the eigenvector convergence by leveraging the eigenvalue convergence results. Our discussion relies on the following identity, which follows from the residual theorem and the spectral decomposition. Specifically, for any positive definite matrix \mathbf{A} admitting spectral decomposition $\mathbf{A} = \sum_{i=1}^n \lambda_i(A) \zeta_i \zeta_i^\top$, we have

$$\zeta_i \zeta_i^\top = \frac{1}{2\pi i} \oint_{\Gamma} (z\mathbf{I} - \mathbf{A})^{-1} dz, \quad (\text{B.9})$$

where $\Gamma \subset \mathbb{C}$ is some simply connected contour only containing $\lambda_i(\mathbf{A})$ and no other eigenvalues. Based on the above representation, we have that

$$\begin{aligned} \langle \mathbf{u}_i, \mathbf{v}_i \rangle^2 &= \frac{1}{2\pi i} \int_{\Gamma_i} \mathbf{v}_i^\top (z\mathbf{I} - n^{-1}\mathbf{K}_x)^{-1} \mathbf{v}_i dz + \frac{1}{2\pi i} \int_{\Gamma_i} \mathbf{v}_i^\top [(z\mathbf{I} - n^{-1}\mathbf{K}_y)^{-1} - (z\mathbf{I} - n^{-1}\mathbf{K}_x)^{-1}] \mathbf{v}_i dz \\ &:= \mathbf{L}_1 + \mathbf{L}_2, \end{aligned} \quad (\text{B.10})$$

for some contour $\Gamma_i := \mathbb{B}(\gamma_i, \frac{r_i}{C})$, for some large constant $C > 0$, where $\mathbb{B}(\gamma_i, \frac{r_i}{C})$ is the disk centered at γ_i with radius r_i/C and we recall $r_i := \min\{\gamma_{i-1} - \gamma_i, \gamma_i - \gamma_{i+1}\}$.

On one hand, by Lemma A.1 and Weyl's inequality, we have

$$|\mu_i - \gamma_i| \leq \|\mathcal{K} - \mathcal{K}_n\| \prec \frac{1}{\sqrt{n}},$$

and the definition of r_i , we conclude that when C is sufficiently large, μ_i is the only simple pole of the resolvent $(z\mathbf{I} - n^{-1}\mathbf{K}_x)^{-1}$ on Γ_i for large enough n . Using the spectral decomposition of $(z\mathbf{I} - n^{-1}\mathbf{K}_x)^{-1}$ and residual theorem, we have that

$$\mathbf{L}_1 = 1. \quad (\text{B.11})$$

On the other hand, the control of \mathbf{L}_2 relies on the resolvent identity (see equation (5.5) of [40]) that

$$(z\mathbf{I} - n^{-1}\mathbf{K}_y)^{-1} - (z\mathbf{I} - n^{-1}\mathbf{K}_x)^{-1} = (z\mathbf{I} - n^{-1}\mathbf{K}_y)^{-1} [n^{-1}\mathbf{K}_y - n^{-1}\mathbf{K}_x] (z\mathbf{I} - n^{-1}\mathbf{K}_x)^{-1}. \quad (\text{B.12})$$

By the definition of Γ_i , using (B.8) and Lemma A.1 (or Part I of Theorem 3.3), we find that

$$\inf_{z \in \Gamma_i} \min\{|\lambda_i - z|, |\lambda_{i-1} - z|, |\lambda_{i+1} - z|\} \asymp r_i,$$

where we used the assumption that $r_i^2 \geq Cn^\epsilon (\frac{1}{\sqrt{n}} + \frac{1}{rn^{\alpha-\beta-1}})$, which implies that for some constant $C_1 > 0$, $r_i \geq C_1 n^{\epsilon/2} (\frac{1}{\sqrt{n}} + \frac{1}{rn^{\alpha-\beta-1}})$ regardless if r_i is less than 1 or not. Moreover, by the definition of the resolvent, we have that

$$\begin{aligned} \sup_{z \in \Gamma_i} \|(z\mathbf{I} - n^{-1}\mathbf{K}_y)^{-1}\| &\leq \sup_{z \in \Gamma_i} \left(\frac{1}{|\lambda_i - z|} + \frac{1}{|\lambda_{i-1} - z|} + \frac{1}{|\lambda_{i+1} - z|} \right) \\ &\prec \frac{1}{r_i}. \end{aligned}$$

Similarly, we can show that

$$\sup_{z \in \Gamma_i} \|(z\mathbf{I} - n^{-1}\mathbf{K}_x)^{-1}\| \prec \frac{1}{r_i}.$$

Together with (B.12) and (B.8), we have that

$$\mathsf{L}_2 \prec \frac{1}{r_i^2} \left[\frac{1}{\sqrt{n}} + \frac{1}{rn^{\alpha-\beta-1}} \right].$$

Insert the above bound and (B.11) back into (B.10), we immediately obtain that

$$|\langle \mathbf{u}_i, \mathbf{v}_i \rangle^2 - 1| \prec \frac{1}{r_i^2} \left[\frac{1}{\sqrt{n}} + \frac{1}{rn^{\alpha-\beta-1}} \right].$$

This completes our proof as $\alpha > \beta + 1$. \square

B.2 Proof of Theorem 3.5

Eigenvalue convergence. By the triangle inequality, we have

$$|\lambda_i - \gamma_i| \leq |\lambda_i - \mu_i| + |\mu_i - \gamma_i|.$$

The first term of the right-hand side of the above equation can be controlled by Theorem 3.2. For the second term, we point out that when h is fixed as in (A.8), we can directly apply Lemma A.1 to obtain the final upper bound. When h is selected according to Algorithm 1 of the main paper, the proof follows from the same argument given Lemma A.4. \square

Eigenfunction convergence. Again, we focus on the setting where the bandwidth is in the form of (A.8). The arguments for bandwidth h_n follows from Lemma A.4 as before. As before, in the following, without loss of generality, we will consider the reduced data $\{\mathbf{y}_i^0\}_{1 \leq i \leq n}$ and their related quantities $\{\mathbf{x}_i^0\}_{1 \leq i \leq n}$ and $\{\mathbf{z}_i^0\}_{1 \leq i \leq n}$. For simplicity, we omit their superscripts and denote them as $\{\mathbf{y}_i\}$, $\{\mathbf{x}_i\}$ and $\{\mathbf{z}_i\}$.

We denote $\mathbf{y} \in \mathbb{R}^n$ as

$$\mathbf{y} = (\mathbf{y}, \mathbf{y}^\perp), \quad \mathbf{y} \in \mathbb{R}^r \text{ and } \mathbf{y}^\perp \in \mathbb{R}^{n-r},$$

and set $\mathbf{z}_i = (\mathbf{z}_i, \mathbf{z}_i^\perp)^\top$ in a similar fashion. Consequently, by the fact that $\mathbf{x}_i = (\mathbf{x}_i, 0, \dots, 0)$, we have that

$$\|\mathbf{y} - \mathbf{y}_i\|_2^2 = \|\mathbf{y} - \mathbf{x}_i\|_2^2 + \|\mathbf{z}_i\|_2^2 + \|\mathbf{y}^\perp\|_2^2 - 2(\mathbf{y}^\perp)^\top \mathbf{z}_i^\perp - 2(\mathbf{y} - \mathbf{x}_i)^\top \mathbf{z}_i.$$

This leads to

$$\exp\left(-\frac{\|\mathbf{y} - \mathbf{y}_i\|_2^2}{h}\right) = \exp\left(-\frac{\|\mathbf{y} - \mathbf{x}_i\|_2^2}{h}\right) \cdot \ell,$$

where ℓ is denoted as

$$\ell := \exp\left(-\frac{\|\mathbf{z}_i\|_2^2 + \|\mathbf{y}^\perp\|_2^2 - 2(\mathbf{y}^\perp)^\top \mathbf{z}_i^\perp - 2(\mathbf{y} - \mathbf{x}_i)^\top \mathbf{z}_i}{h}\right).$$

As we will examine the RKHS norm in \mathcal{H}_K , containing functions defined only on the support of $\tilde{\mathbb{P}}$, without loss of generality, we can ignore \mathbf{y}^\perp (that is, set $\mathbf{y}^\perp = 0$) and only focus on \mathbf{y} . Since \mathbf{y} is sub-Gaussian, using the elementary estimate $\exp(-x) \sim 1 - x$ as $x \rightarrow 0$, it is easy to see that

$$\ell = 1 + \mathsf{O}_{\prec}(r^{-1/2}n^{-\frac{\alpha-\beta}{2}} + r^{-1}n^{-(\alpha-\beta-1)}),$$

uniformly in \mathbf{y} on the support of $\tilde{\mathcal{P}}$. This immediately shows that

$$\exp\left(-\frac{\|\mathbf{y} - \mathbf{y}_i\|_2^2}{h}\right) = \exp\left(-\frac{\|\mathbf{y} - \mathbf{x}_i\|_2^2}{h}\right) + \mathcal{O}_{\prec}(r^{-1/2}n^{-\frac{\alpha-\beta}{2}} + r^{-1}n^{-(\alpha-\beta-1)}). \quad (\text{B.13})$$

With the above preparation, we start analyzing the eigenfunctions. Recall the definition in (A.4). In the first step, we study the following term

$$\left(\widehat{\phi}_i^{(n)}(\mathbf{y}) - \phi_i^{(n)}(\mathbf{y})\right)^2 = (\mathbf{E}_1 + \mathbf{E}_2 + \mathbf{E}_3)^2, \quad (\text{B.14})$$

where $\mathbf{E}_k, k = 1, 2, 3$, are denoted as follows

$$\begin{aligned} \mathbf{E}_1 &:= \left(\frac{1}{\lambda_i} - \frac{1}{\mu_i}\right) \frac{1}{\sqrt{n}} \sum_{j=1}^n \exp\left(-\frac{\|\mathbf{y} - \mathbf{y}_j\|_2^2}{h}\right) v_{ij}, \\ \mathbf{E}_2 &:= \frac{1}{\sqrt{n}\mu_i} \sum_{j=1}^n \left[\exp\left(-\frac{\|\mathbf{y} - \mathbf{y}_j\|_2^2}{h}\right) - \exp\left(-\frac{\|\mathbf{y} - \mathbf{x}_j\|_2^2}{h}\right) \right] v_{ij}, \\ \mathbf{E}_3 &:= \frac{1}{\sqrt{n}\mu_i} \sum_{j=1}^n \exp\left(-\frac{\|\mathbf{y} - \mathbf{x}_j\|_2^2}{h}\right) (v_{ij} - u_{ij}). \end{aligned}$$

First, by Theorem 3.2, when $1 \leq i \leq K$, we have that

$$\left| \frac{1}{\lambda_i} - \frac{1}{\mu_i} \right| \prec \frac{|\lambda_i - \mu_i|}{\lambda_i \mu_i} \prec \frac{1}{\mu_i} \left(\frac{1}{\sqrt{n}} + \frac{1}{rn^{\alpha-\beta-1}} \right).$$

Consequently, using the boundedness of the kernels and the fact that $\|\mathbf{v}\|_1 \leq \sqrt{n}\|\mathbf{v}\|_2 = \sqrt{n}$, we conclude that for $i \leq K$

$$\mathbf{E}_1 \prec \frac{1}{\mu_i} \left(\frac{1}{\sqrt{n}} + \frac{1}{rn^{\alpha-\beta-1}} \right).$$

Second, by (B.13), we readily have that for $i \leq K$

$$\mathbf{E}_2 \prec \frac{1}{\mu_i} \left(\frac{1}{\sqrt{rn}^{\frac{\alpha-\beta}{2}}} + \frac{1}{rn^{\alpha-\beta-1}} \right).$$

Third, we control \mathbf{E}_3 . On one hand, for $i \leq K$, by Lemma A.1, we have that $\mathbf{E}_3 = \mathcal{O}(1)$. On the other hand, by setting

$$\mathbf{a} = (a_1, \dots, a_n)^\top, \quad \mathbf{b} = (b_1, \dots, b_n)^\top,$$

where $a_i = \frac{1}{\sqrt{n}\mu_i} \exp\left(-\frac{\|\mathbf{y} - \mathbf{x}_j\|_2^2}{h}\right)$ and $b_i = v_{ij} - u_{ij}$, we can rewrite

$$\mathbf{E}_3^2 = \mathbf{b}^\top \mathbf{a} \mathbf{a}^\top \mathbf{b}.$$

Note that $\|\mathbf{b}\|_2^2 = \|\mathbf{v}_i - \mathbf{u}_i\|_2^2$. Then we have that

$$\mathbf{E}_3^2 \leq \|\mathbf{a}\|_2^2 \|\mathbf{b}\|_2^2 \prec \frac{1}{\mu_i^2} \left(\left[\frac{1}{\sqrt{n}} + \frac{1}{rn^{\alpha-\beta-1}} \right] \frac{1}{r_i^2} \right),$$

where in the second step we used Part II of Theorem 3.2. Combining all the above bounds, using (B.14), when $i \leq K$, we arrive at

$$\mu_i \left(\widehat{\phi}_i^{(n)}(\mathbf{y}) - \phi_i^{(n)}(\mathbf{y}) \right)^2 \prec \left[\frac{1}{\sqrt{n}} + \frac{1}{rn^{\alpha-\beta-1}} \right]^2 + \left[\frac{1}{\sqrt{n}} + \frac{1}{rn^{\alpha-\beta-1}} \right] \frac{1}{r_i^2}, \quad (\text{B.15})$$

uniformly in \mathbf{y} on the support of $\widetilde{\mathcal{P}}$. To see $\widehat{\phi}_i^{(n)}$ has finite K -norm, we note that for $i \leq K$,

$$\|\widehat{\phi}_i^{(n)}\|_K \leq \|\phi_i^{(n)}\|_K + \|\widehat{\phi}_i^{(n)} - \phi_i^{(n)}\|_K \leq \frac{1}{\sqrt{\mu_i}} + \frac{1}{\sqrt{\mu_i}} \left[\frac{1}{\sqrt{n}} + \frac{1}{rn^{\alpha-\beta-1}} + \left[\frac{1}{\sqrt{n}} + \frac{1}{rn^{\alpha-\beta-1}} \right]^{1/2} \frac{1}{r_i} \right] \prec 1.$$

Finally, since by Part I of Theorem 3.2, we have

$$\|\sqrt{\lambda_i} \phi_i^{(n)} - \sqrt{\mu_i} \phi_i^{(n)}\|_K \leq (\sqrt{\lambda_i} - \sqrt{\mu_i}) \|\phi_i^{(n)}\|_K \leq \frac{\sqrt{\lambda_i} - \sqrt{\mu_i}}{\sqrt{\mu_i}} \|\sqrt{\mu_i} \phi_i^{(n)}\|_K \prec \frac{1}{\sqrt{n}} + \frac{1}{rn^{\alpha-\beta-1}},$$

and similarly

$$\|\sqrt{\lambda_i} \widehat{\phi}_i^{(n)} - \sqrt{\mu_i} \widehat{\phi}_i^{(n)}\|_K \leq (\sqrt{\lambda_i} - \sqrt{\mu_i}) \|\widehat{\phi}_i^{(n)}\|_K \prec \frac{1}{\sqrt{n}} + \frac{1}{rn^{\alpha-\beta-1}},$$

then we have

$$\begin{aligned} \|\sqrt{\lambda_i} \widehat{\phi}_i^{(n)} - \sqrt{\gamma_i} \widetilde{\phi}_i\|_K &\leq \|\sqrt{\lambda_i} \widehat{\phi}_i^{(n)} - \sqrt{\lambda_i} \phi_i^{(n)}\|_K + \|\sqrt{\lambda_i} \phi_i^{(n)} - \sqrt{\mu_i} \phi_i^{(n)}\|_K + \|\sqrt{\mu_i} \phi_i^{(n)} - \sqrt{\gamma_i} \widetilde{\phi}_i\|_K \\ &\leq \|\sqrt{\mu_i} \widehat{\phi}_i^{(n)} - \sqrt{\mu_i} \phi_i^{(n)}\|_K + \|\sqrt{\lambda_i} \widehat{\phi}_i^{(n)} - \sqrt{\mu_i} \widehat{\phi}_i^{(n)}\|_K + 2\|\sqrt{\lambda_i} \phi_i^{(n)} - \sqrt{\mu_i} \phi_i^{(n)}\|_K \\ &\quad + \|\sqrt{\mu_i} \phi_i^{(n)} - \sqrt{\gamma_i} \widetilde{\phi}_i\|_K \\ &\prec \|\sqrt{\mu_i} \widehat{\phi}_i^{(n)} - \sqrt{\mu_i} \phi_i^{(n)}\|_K + \frac{1}{\sqrt{n}} + \frac{1}{rn^{\alpha-\beta-1}} + \frac{1}{\sqrt{nr_i}}. \end{aligned}$$

where in the last inequality we used Lemma A.1. Finally, plugging in (B.15), we obtain the final result as $i \leq K$. \square

C Some Results on Gaussian Integral Operators

In this section, we collect some results on integral operators. Consider a special case when $\{\mathbf{x}_i\}$ are Gaussian. In such a setting, the eigenvalues and eigenfunctions of the integral operator can be calculated explicitly. We first state the results when $r = 1$. Let $\mathbf{p}(x)$ be the density function of $\mathcal{N}(0, \sigma^2)$ random variable. For the ease of statement, we write the Gaussian kernel function that

$$k(x, y) = e^{-\frac{\|x-y\|_2^2}{2h}}, \quad (\text{C.1})$$

for some fixed bandwidth h . Consequently, we can construct the following integral operator

$$\mathcal{K}_1^\sigma f(x) = \int k(x, y) f(y) \mathbf{p}(y) dy.$$

Denote $\{\gamma_i\}$ and $\{\phi_i(x)\}$ as the sequence of the eigenvalues and eigenfunctions of \mathcal{K}_1^σ so that

$$\mathcal{K}_1^\sigma \phi_i(x) = \gamma_i \phi_i(x), \quad \int \phi_i^2(x) \mathbf{p}(x) dx = 1.$$

Note that the eigenfunctions are in fact defined in \mathbb{R} via the relation that

$$\phi_i(x) = \frac{1}{\gamma_i} \int k(x, y) \phi_i(y) \mathbf{p}(y) dy, \text{ if } \lambda_i > 0.$$

The following lemma provides the exact form for the eigenvalues and eigenfunctions under this setting.

Lemma C.1. *Denote $\beta = 2\sigma^2/h$. The eigenvalues and eigenfunctions for \mathcal{K}_1^σ are given by*

$$\gamma_i = \frac{\sqrt{2}}{\sqrt{1 + \beta + \sqrt{1 + 2\beta}}} \left(\frac{\beta}{1 + \beta + \sqrt{1 + 2\beta}} \right)^i, \quad (\text{C.2})$$

$$\phi_i(x) = \frac{(1 + 2\beta)^{1/8}}{\sqrt{2^i i!}} \exp\left(-\frac{x^2}{2\sigma^2} \frac{\sqrt{1 + 2\beta} - 1}{2}\right) H_i\left(\left(\frac{1}{4} + \frac{\beta}{2}\right)^{1/4} \frac{x}{\sigma}\right), \quad (\text{C.3})$$

where $H_i(\cdot)$ is the i th order Hermite polynomial.

Proof. See Proposition 1 of [58]. □

The above results can also be generalized to the r -dimensional setting when $\mathbf{p}(\mathbf{x})$ is the density function of $\mathcal{N}(\mathbf{0}, \Sigma)$ where Σ is a diagonal matrix so that

$$\Sigma = \text{diag}\{\theta_1, \dots, \theta_r\}, \quad \text{where } \theta_i = \sigma_i^2$$

Due to invariance of the kernel, the associated integral operator, denoted as \mathcal{K}_r , has a direct sum decomposition

$$\mathcal{K}_r = \bigoplus_{i=1}^r \mathcal{K}_1^{\sigma_i}.$$

Analogously, the eigenvalues and eigenfunctions of \mathcal{K}_r can also be calculated explicitly as follows. Recall that for given two operators \mathcal{F}_1 and \mathcal{F}_2 , the spectrum of their direct sum $\mathcal{F}_1 \oplus \mathcal{F}_2$ consists of pairwise products $\gamma_i(\mathcal{F}_1)\gamma_j(\mathcal{F}_2)$. Moreover, the eigenfunction of the product can be written into a multindex form so that corresponding to $\gamma_i(\mathcal{F}_1)\gamma_j(\mathcal{F}_2)$, we have

$$\phi_{[i,j]}(x_1, x_2) = \phi_i(x_1)\psi_j(x_2),$$

where $\{\phi_i(x)\}$ and $\{\psi_j(x)\}$ are the eigenfunctions of the operators \mathcal{F}_1 and \mathcal{F}_2 , respectively. Consequently, we can obtain the following results.

Lemma C.2. *Denote $\beta_i = 2\sigma_i^2/h$. Then the eigenvalues and eigenfunctions of \mathcal{K}_r can be represented using the multindex over all components, i.e.,*

$$\gamma_{[i_1, i_2, \dots, i_r]} = \prod_{j=1}^r \gamma_{i_j}(\mathcal{K}_1^{\sigma_j}),$$

and for $\mathbf{x} = (x_1, x_2, \dots, x_r)$

$$\phi_{[i_1, i_2, \dots, i_r]}(\mathbf{x}) = \prod_{j=1}^r \phi_{i_j}(\mathcal{K}_1^{\sigma_j})(x_j).$$

Proof. See Section 3 of [57]. □

D Tuning Parameter Selection and Additional Simulation Results

D.1 A Resampling Method for Selecting Quantile ω in (2.2)

A resampling-based algorithm for determining the quantile parameter was proposed in Algorithm 1 of [20]. The method provides a choice of \mathbf{s} using resampling method to distinguish the larger outlier eigenvalues and bulk eigenvalues of the kernel matrix \mathbf{K}_n , where the outlier eigenvalues stand for the signal parts and bulk eigenvalues are for the noise part. A key observation underlying this approach is that the bulk eigenvalues are close to each other so that the ratios of two consecutive eigenvalues are close to one (see Remark 2.9 of [20] for more details). Given the choice of \mathbf{s} , the algorithm is summarized below for self-completeness.

1. For a prechosen sequence of quantiles $\{\omega\}_{i=1}^T$, calculate the associated bandwidths according to (2.2), denoted as $\{h_i\}_{i=1}^T$.
2. For each $1 \leq i \leq T$, calculate the eigenvalues of the kernel matrices $\mathbf{K}_{n,i}$ which is conducted using the bandwidth h_i . Denote the eigenvalues of $\mathbf{K}_{n,i}$ in the decreasing order as $\{\lambda_k^{(i)}\}_{k=1}^n$.
3. For some $\mathbf{s} > 0$, denote

$$k(\omega_i) := \max_{1 \leq k \leq n-1} \left\{ k \left| \frac{\lambda_k^{(i)}}{\lambda_{k+1}^{(i)}} \geq 1 + \mathbf{s} \right. \right\}.$$

Choose the quantile ω such that

$$\omega = \max_i \left[\operatorname{argmax}_{\omega_i} k(\omega_i) \right]. \quad (\text{D.1})$$

In particular, the last step can be replaced by other criteria according to users' purpose. Here we choose the largest one for the purpose of robustness. To demonstrate the empirical performance of the proposed quantile selection algorithm, we consider the three examples in Section 4.1, and evaluate the performance of the proposed embedding method under the quantile chosen by (D.1), across a variety of signal-to-noise ratios. In each setting, we used $\mathbf{s} = 0.35$ according to [20]. Again, the performance is measured by the concordance between the low-dimensional embeddings and the original low-dimensional noiseless samples. As a comparison, we also include the embeddings obtained from (i) the fixed bandwidth $h = p$, and (ii) the bandwidth selection method proposed by [58]. From Figure 7, we observe that in most cases the bandwidth associated with the quantile (D.1) leads to a much better embedding than the alternative bandwidths. In Figure 8, we show the corresponding ω selected by the resampling method in each example. These results indicate the usefulness and robustness of the quantile selection algorithm.

D.2 Additional Results for Real Data Applications

We include additional figures (Figures 9 and 10) for the real data analysis of the main paper, where the quantile parameter $\omega \in \{0.25, 0.75\}$. The results along with those in Section 4.2 indicate that the proposed method and its advantage over the alternative methods is insensitive to the value of ω .

References

- [1] E. Adeli, G. Wu, B. Saghafi, L. An, F. Shi, and D. Shen. Kernel-based joint feature selection and max-margin classification for early diagnosis of Parkinson's disease. *Scientific Reports*, 7(1):1–14, 2017.

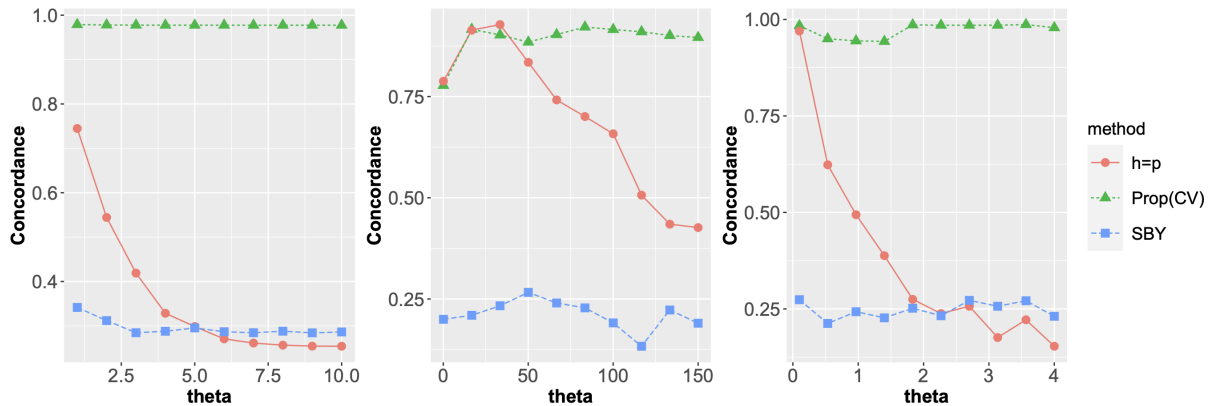


Figure 7: Comparison of bandwidth selection methods through the concordance as in (4.1). Left: the nested sphere mixture manifold; Middle: the “smiley face” manifold; Right: the “mammoth” manifold. Prop(CV) means that we apply Algorithm 1 using the quantile ω from (D.1).

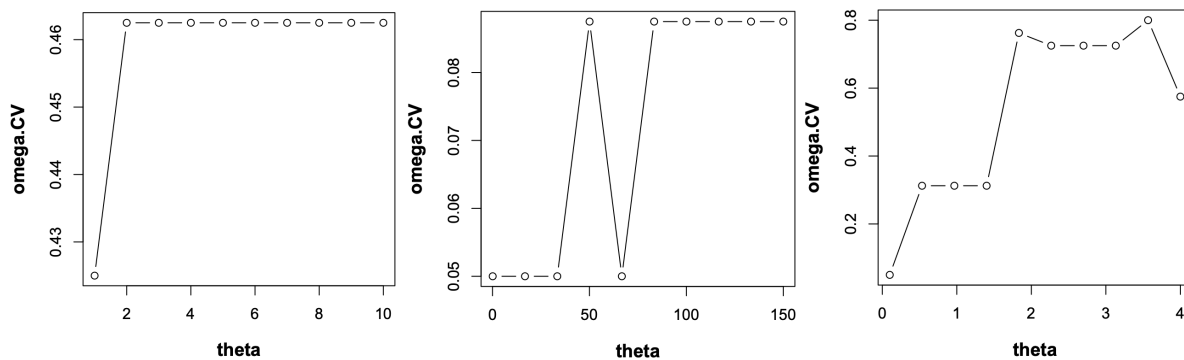


Figure 8: Scatter plots of the resampling selected ω values and the corresponding θ values. Left: the nested sphere mixture manifold; Middle: the “smiley face” manifold; Right: the “mammoth” manifold. ω .CV is the quantile ω chosen by (D.1).

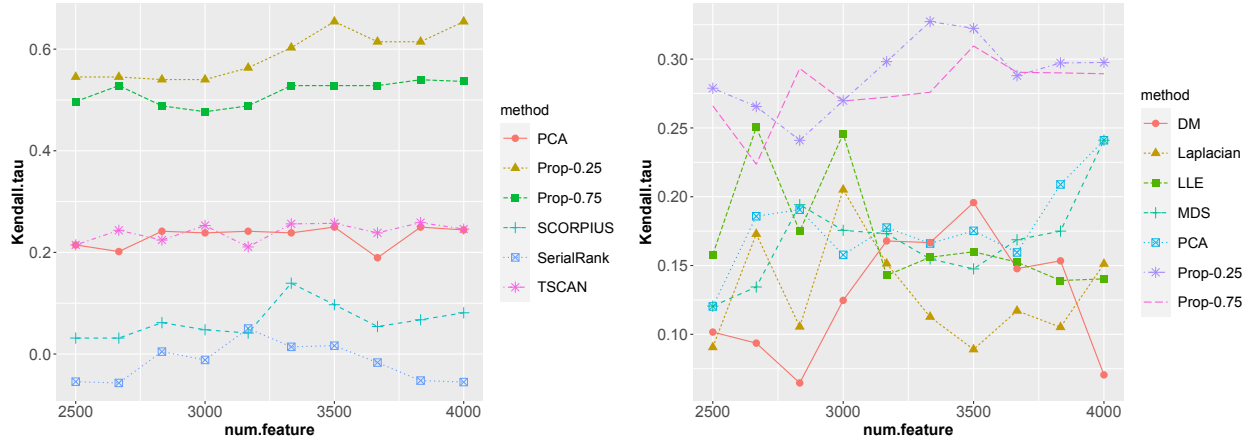


Figure 9: Left: comparison of six methods for cell ordering in Section 4.2.1. Right: comparison of six methods for cell cycle reconstruction in Section 4.2.2. In both plots, the proposed method uses $\omega \in \{0.25, 0.75\}$.

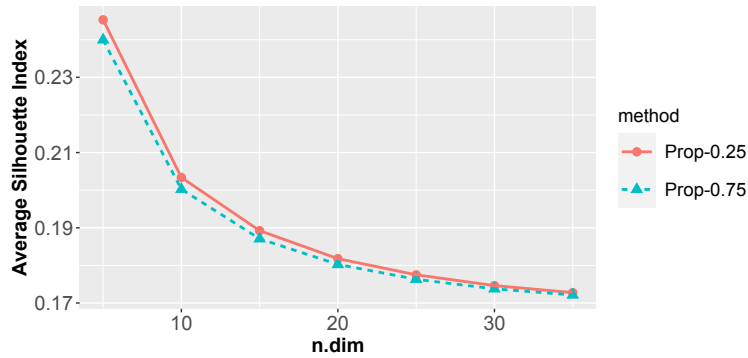


Figure 10: Comparison of average Silhouette indices of the final embeddings of $n = 3946$ samples from the MNIST data, where the quantile parameter $\omega \in \{0.25, 0.75\}$. Combined with Figure 6, we can see that our Algorithm 1 is insensitive to the choice of ω .

- [2] A. A. Amini and Z. S. Razaee. Concentration of kernel matrices with application to kernel spectral clustering. *The Annals of Statistics*, 49(1):531–556, 2021.
- [3] E. Arias-Castro and B. Pelletier. On the convergence of maximum variance unfolding. *Journal of Machine Learning Research*, 14(7), 2013.
- [4] S. Arora, W. Hu, and P. K. Kothari. An analysis of the t-sne algorithm for data visualization. In *Conference On Learning Theory*, pages 1455–1462. PMLR, 2018.
- [5] Z. Bao, X. Ding, J. Wang, and K. Wang. Statistical inference for principal components of spiked covariance matrices. *The Annals of Statistics (in press)*, 2020.
- [6] M. Belkin and P. Niyogi. Laplacian Eigenmaps for Dimensionality Reduction and Data Representation. *Neural. Comput.*, 15(6):1373–1396, 2003.
- [7] M. Belkin and P. Niyogi. Convergence of Laplacian eigenmaps. *Advances in Neural Information Processing Systems*, 19:129, 2007.
- [8] A. Berlinet and C. Thomas-Agnan. *Reproducing kernel Hilbert spaces in probability and statistics*. Springer Science & Business Media, 2011.
- [9] C. M. Bishop. *Pattern recognition and machine learning*. 2006.
- [10] G. Blanchard, O. Bousquet, and L. Zwald. Statistical properties of kernel principal component analysis. *Machine Learning*, 66(2):259–294, 2007.
- [11] C. Bordenave. On Euclidean random matrices in high dimension. *Electronic Communications in Probability*, 18:1–8, 2013.
- [12] I. Borg and P. J. Groenen. *Modern multidimensional scaling: Theory and applications*. Springer Science & Business Media, 2005.
- [13] M. L. Braun. Accurate error bounds for the eigenvalues of the kernel matrix. *Journal of Machine Learning Research*, 7(82):2303–2328, 2006.
- [14] T. T. Cai and R. Ma. Theoretical foundations of t-sne for visualizing high-dimensional clustered data. *arXiv preprint arXiv:2105.07536*, 2021.
- [15] J. Calder, N. G. Trillos, and M. Lewicka. Lipschitz regularity of graph Laplacians on random data clouds. *arXiv preprint arXiv:2007.06679*, 2020.
- [16] R. Cannoodt, W. Saelens, D. Sichien, S. Tavernier, S. Janssens, M. Guillems, B. Lambrecht, K. De Preter, and Y. Saeys. SCORPIUS improves trajectory inference and identifies novel modules in dendritic cell development. *bioRxiv*, page 079509, 2016.
- [17] M.-Y. Cheng and H.-T. Wu. Local linear regression on manifolds and its geometric interpretation. *Journal of the American Statistical Association*, 108(504):1421–1434, 2013.
- [18] X. Cheng and A. Singer. The spectrum of random inner-product kernel matrices. *Random Matrices: Theory and Applications*, 2(04):1350010, 2013.

- [19] R. R. Coifman and S. Lafon. Diffusion maps. *Applied and Computational Harmonic Analysis*, 21(1):5–30, 2006.
- [20] X. Ding and H.-T. Wu. Impact of signal-to-noise ratio and bandwidth on graph Laplacian spectrum from high-dimensional noisy point cloud. *arXiv preprint arXiv 2011.10725*, 2020.
- [21] X. Ding and H.-T. Wu. On the spectral property of kernel-based sensor fusion algorithms of high dimensional data. *IEEE Transactions on Information Theory*, 67(1):640–670, 2021.
- [22] Y. Do and V. Vu. The spectrum of random kernel matrices: universality results for rough and varying kernels. *Random Matrices: Theory and Applications*, 2(03):1350005, 2013.
- [23] D. L. Donoho and C. Grimes. Hessian eigenmaps: Locally linear embedding techniques for high-dimensional data. *Proceedings of the National Academy of Sciences*, 100(10):5591–5596, 2003.
- [24] D. B. Dunson, H.-T. Wu, and N. Wu. Spectral convergence of graph Laplacian and heat kernel reconstruction in L_∞ from random samples. *Applied and Computational Harmonic Analysis*, 55:282–336, 2021.
- [25] N. El Karoui. On information plus noise kernel random matrices. *The Annals of Statistics*, 38(5):3191–3216, 2010.
- [26] N. El Karoui. The spectrum of kernel random matrices. *The Annals of Statistics*, 38(1):1–50, 2010.
- [27] N. El Karoui and H.-T. Wu. Connection graph Laplacian methods can be made robust to noise. *Ann. Statist.*, 44(1):346–372, 2016.
- [28] J. Fan, W. Wang, and Y. Zhong. An ℓ_∞ eigenvector perturbation bound and its application to robust covariance estimation. *Journal of Machine Learning Research*, 18(207):1–42, 2018.
- [29] Z. Fan and A. Montanari. The spectral norm of random inner-product kernel matrices. *Probability Theory and Related Fields*, 173(1):27–85, 2019.
- [30] F. Fogel, A. d’Aspremont, and M. Vojnovic. Serialrank: Spectral ranking using seriation. *Advances in Neural Information Processing Systems*, 27:900–908, 2014.
- [31] N. García Trillos, M. Gerlach, M. Hein, and D. Slepcev. Error estimates for spectral convergence of the graph Laplacian on random geometric graphs toward the Laplace-Beltrami operator. *Found. Comput. Math.*, 20(4):827–887, 2020.
- [32] E. Giné and V. Koltchinskii. Empirical graph Laplacian approximation of Laplace–Beltrami operators: Large sample results. In *High dimensional probability*, pages 238–259. Institute of Mathematical Statistics, 2006.
- [33] F. Guo, L. Yan, H. Guo, L. Li, B. Hu, Y. Zhao, J. Yong, Y. Hu, X. Wang, Y. Wei, et al. The transcriptome and DNA methylome landscapes of human primordial germ cells. *Cell*, 161(6):1437–1452, 2015.
- [34] T. Hofmann, B. Schölkopf, and A. J. Smola. Kernel methods in machine learning. *The Annals of Statistics*, 36(3):1171–1220, 2008.

- [35] R. Horn and C. Johnson. *Matrix Analysis*. Cambridge University Press, 2nd edition, 2012.
- [36] Z. Ji and H. Ji. TSCAN: Pseudo-time reconstruction and evaluation in single-cell RNA-seq analysis. *Nucleic Acids Research*, 44(13):e117–e117, 2016.
- [37] I. M. Johnstone. On the distribution of the largest eigenvalue in principal components analysis. *The Annals of statistics*, 29(2):295–327, 2001.
- [38] I. Jolliffe. *Principal Component Analysis*. Springer Series in Statistics. 2002.
- [39] K. Jörgens. *Linear integral operators*, volume 13. Pitman Advanced Publishing Program, 1982.
- [40] T. Kato. *A short introduction to perturbation theory for linear operators*. Springer-Verlag, New York-Berlin, 1982.
- [41] D. Kobak and P. Berens. The art of using t-SNE for single-cell transcriptomics. *Nature Communications*, 10(1):1–14, 2019.
- [42] V. Koltchinskii and E. Giné. Random matrix approximation of spectra of integral operators. *Bernoulli*, 6(1):113 – 167, 2000.
- [43] S. Y. Kung. *Kernel methods and machine learning*. Cambridge University Press, 2014.
- [44] J. A. Lee and M. Verleysen. *Nonlinear dimensionality reduction*. Springer, 2007.
- [45] G. C. Linderman and S. Steinerberger. Clustering with t-SNE, provably. *SIAM Journal on Mathematics of Data Science*, 1(2):313–332, 2019.
- [46] J. H. Manton, P.-O. Amblard, et al. A primer on reproducing kernel hilbert spaces. *Foundations and Trends® in Signal Processing*, 8(1–2):1–126, 2015.
- [47] V. A. Marčenko and L. A. Pastur. Distribution of eigenvalues for some sets of random matrices. *Mathematics of the USSR-Sbornik*, 1(4):457, 1967.
- [48] L. McInnes, J. Healy, and J. Melville. Umap: Uniform manifold approximation and projection for dimension reduction. *arXiv preprint arXiv:1802.03426*, 2018.
- [49] K. R. Moon, D. van Dijk, Z. Wang, S. Gigante, D. B. Burkhardt, W. S. Chen, K. Yim, A. van den Elzen, M. J. Hirn, R. R. Coifman, et al. Visualizing structure and transitions in high-dimensional biological data. *Nature Biotechnology*, 37(12):1482–1492, 2019.
- [50] J. Nash. The imbedding problem for Riemannian manifolds. *Ann. of Math.*, 63:20–63, 1956.
- [51] L. Rosasco, M. Belkin, and E. D. Vito. On learning with integral operators. *Journal of Machine Learning Research*, 11(30):905–934, 2010.
- [52] P. J. Rousseeuw. Silhouettes: a graphical aid to the interpretation and validation of cluster analysis. *Journal of Computational and Applied Mathematics*, 20:53–65, 1987.
- [53] S. T. Roweis and L. K. Saul. Nonlinear dimensionality reduction by locally linear embedding. *Science*, 290(5500):2323–2326, 2000.

- [54] B. Schölkopf and A. Smola. *Learning with Kernels: Support Vector Machines, Regularization, Optimization, and Beyond*. Adaptive computation and machine learning. MIT Press, 2002.
- [55] B. Schölkopf, A. Smola, and K.-R. Müller. Nonlinear component analysis as a kernel eigenvalue problem. *Neural Computation*, 10(5):1299–1319, 1998.
- [56] J. Shawe-Taylor, N. Cristianini, et al. *Kernel methods for pattern analysis*. Cambridge university press, 2004.
- [57] T. Shi, M. Belkin, and B. Yu. Data spectroscopy: Learning mixture models using eigenspaces of convolution operators. In *Proceedings of the 25th International Conference on Machine Learning, ICML '08*, page 936–943, 2008.
- [58] T. Shi, M. Belkin, and B. Yu. Data spectroscopy: Eigenspaces of convolution operators and clustering. *The Annals of Statistics*, 37(6B):3960 – 3984, 2009.
- [59] Y. Shiokawa, Y. Date, and J. Kikuchi. Application of kernel principal component analysis and computational machine learning to exploration of metabolites strongly associated with diet. *Scientific Reports*, 8(1):1–8, 2018.
- [60] A. Singer. From graph to manifold Laplacian: The convergence rate. *Applied and Computational Harmonic Analysis*, 21(1):128–134, 2006.
- [61] A. Singer and H.-T. Wu. Vector diffusion maps and the connection Laplacian. *Communications on pure and applied mathematics*, 65(8):1067–1144, 2012.
- [62] A. Singer and H.-T. Wu. Spectral convergence of the connection Laplacian from random samples. *Information and Inference: A Journal of the IMA*, 6(1):58–123, 2017.
- [63] S. Smale and D.-X. Zhou. Learning theory estimates via integral operators and their approximations. *Constructive Approximation*, 26:153–172, 2007.
- [64] S. Smale and D.-X. Zhou. Geometry on probability spaces. *Constr. Approx.*, 30(3):311–323, 2009.
- [65] A. Smith, H. Zha, and X.-m. Wu. Convergence and rate of convergence of a manifold-based dimension reduction algorithm. In *Advances in Neural Information Processing Systems*, volume 21, 2008.
- [66] J. B. Tenenbaum, V. d. Silva, and J. C. Langford. A global geometric framework for nonlinear dimensionality reduction. *Science*, 290(5500):2319–2323, 2000.
- [67] L. Van der Maaten and G. Hinton. Visualizing data using t-sne. *Journal of Machine Learning Research*, 9(11), 2008.
- [68] L. Van Der Maaten, E. Postma, and J. Van den Herik. Dimensionality reduction: A comparative review. *J Mach Learn Res*, 10(66-71):13, 2009.
- [69] U. von Luxburg. A tutorial on spectral clustering. *Statistics and computing*, 17(4):395–416, 2007.
- [70] U. von Luxburg, M. Belkin, and O. Bousquet. Consistency of spectral clustering. *The Annals of Statistics*, 36(2):555–586, 2008.

- [71] U. von Luxburg, O. Bousquet, and M. Belkin. On the convergence of spectral clustering on random samples: the normalized case. In *International Conference on Computational Learning Theory*, pages 457–471, 2004.
- [72] B. Wang, J. Zhu, E. Pierson, D. Ramazzotti, and S. Batzoglou. Visualization and analysis of single-cell RNA-seq data by kernel-based similarity learning. *Nature Methods*, 14(4):414–416, 2017.
- [73] K. Q. Weinberger and L. K. Saul. An introduction to nonlinear dimensionality reduction by maximum variance unfolding. In *AAAI*, volume 6, pages 1683–1686, 2006.
- [74] C. L. Wormell and S. Reich. Spectral convergence of diffusion maps: Improved error bounds and an alternative normalization. *SIAM Journal on Numerical Analysis*, 59(3):1687–1734, 2021.
- [75] H.-T. Wu and N. Wu. Think globally, fit locally under the manifold setup: Asymptotic analysis of locally linear embedding. *The Annals of Statistics*, 46(6B):3805–3837, 2018.
- [76] Z. Zhang and H. Zha. Principal manifolds and nonlinear dimensionality reduction via tangent space alignment. *SIAM journal on scientific computing*, 26(1):313–338, 2004.
- [77] Z. Zhou and A. A.Amini. Analysis of spectral clustering algorithms for community detection: the general bipartite setting. *Journal of Machine Learning Research*, 20(47):1–47, 2019.